

UNRAVELLING THE ELECTROCATALYTIC ACTIVITY OF LaFeO_3 TOWARDS OXYGEN REDUCTION REACTION

M.Sc. Thesis

By
KASHIKA KHATRI



DISCIPLINE OF PHYSICS
INDIAN INSTITUTE OF TECHNOLOGY INDORE
MAY 2024

UNRAVELLING THE ELECTROCATALYTIC ACTIVITY OF LaFeO_3 TOWARDS OXYGEN REDUCTION REACTION

A THESIS

*Submitted in partial fulfillment of the
requirements for the award of the degree
of*
Master of Science

by
KASHIKA KHATRI



DISCIPLINE OF PHYSICS
INDIAN INSTITUTE OF TECHNOLOGY INDORE
MAY 2024



INDIAN INSTITUTE OF TECHNOLOGY INDORE

CANDIDATE'S DECLARATION

I hereby certify that the work which is being presented in the thesis entitled **UNRAVELLING THE ELECTROCATALYTIC ACTIVITY OF LaFeO_3 TOWARDS OXYGEN REDUCTION REACTION** in the partial fulfilment of the requirements for the award of the degree of **MASTER OF SCIENCE** and submitted in the **DISCIPLINE OF PHYSICS, Indian Institute of Technology Indore**, is an authentic record of my own work carried out during the time period from July 2022 to May 2024 under the supervision of Dr. Srimanta Pakhira, Associate Professor, Department of Physics, Indian Institute of Technology Indore.

The matter presented in this thesis has not been submitted by me for the award of any other degree of this or any other institute.



24/5/2024

Signature of the student with date
(KASHIKA KHATRI)

This is to certify that the above statement made by the candidate is correct to the best of my/our knowledge.



24th May, 2024
Signature of the Supervisor of M.Sc. thesis
(DR. SRIMANTA PAKHIRA)

KASHIKA KHATRI has successfully given her M.Sc. Oral Examination held on **May 14, 2024**.



Signature of Supervisor of MSc thesis
Date: 24th May, 2024



Convener, DPGC
Date: 24/5/2024

ACKNOWLEDGEMENTS

I extend my heartfelt gratitude to my supervisor, Dr. Srimanta Pakhira, for his unwavering support and guidance throughout the duration of my project. His kindness, patience, and willingness to address all my questions, no matter how trivial, have been invaluable to me. I am truly thankful for his mentorship and encouragement throughout this journey.

I would also like to express my sincere thanks to all my lab mates for their assistance and collaboration whenever I sought their help. Their companionship and willingness to lend a helping hand have greatly enriched my research experience.

Furthermore, I am deeply grateful to my friends and family for their constant emotional support and encouragement. Their presence has provided me with the strength and motivation to persevere through challenges. I am especially thankful to my friends at IIT Indore, whose companionship and positivity have been a source of light and laughter during difficult times. Their friendship has made this academic journey all the more rewarding.

Thank you to everyone who has contributed to this thesis in one way or another. Your support and encouragement have been instrumental in making this accomplishment possible.

ABSTRACT

The oxygen reduction reaction (ORR) is an important process in renewable energy technology such as in fuel cells. The main challenge with fuel cells is the sluggish reaction kinetics of O_2 reduction, and to speed this up studies have been conducted to find an efficient and economical electrocatalyst. In the present work, we theoretically investigated the equilibrium structure and properties of the 3D bulk $LaFeO_3$ perovskite using the GGA+U method implemented in Vienna *Ab initio* Simulation Package (VASP). Thereafter, we cleaved a (001) plane from the bulk $LaFeO_3$ material and computationally modelled a 2D monolayer of $LaFeO_3$. This 2D monolayer of $LaFeO_3$ showed a band gap of 0 eV which depicts that it has the potential to be used as an electrocatalyst for fuel cell applications. Here, the complete ORR pathway has been explored on the surface of 2D monolayer $LaFeO_3$ by employing the First-principles Density Functional Theory (DFT) methods implemented in the VASP code. Both, the associative and the dissociative reaction mechanisms have been explored by computing the change in Gibbs Free Energy (ΔG) for all the reaction steps of ORR. The present study reveals that 2D monolayer $LaFeO_3$ exhibits exceptional electrocatalytic activity and favors the $4e^-$ associative mechanism over the dissociative one. This study proposes that 2D monolayer $LaFeO_3$ can serve as an alternate ORR electrocatalyst to expensive platinum (Pt) in fuel cells.

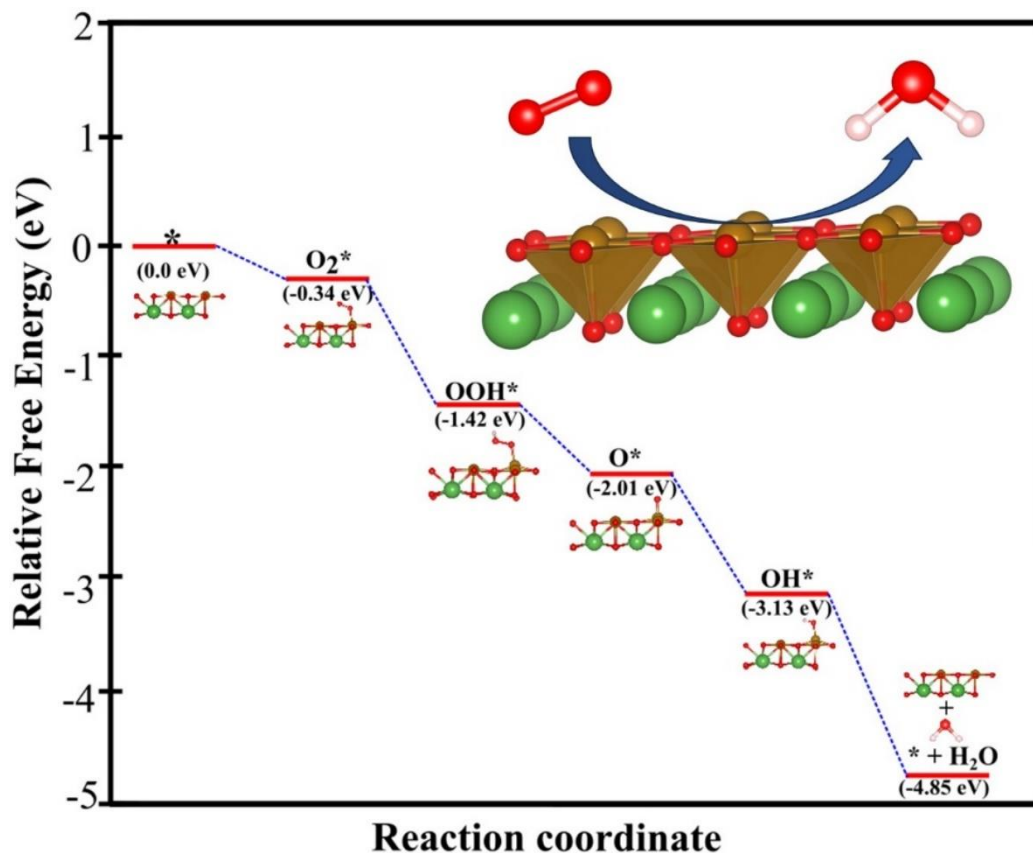


TABLE OF CONTENTS

LIST OF FIGURES

LIST OF TABLES

ACRONYMS

Chapter 1: Introduction

- 1.1 Motivation
- 1.2 Fuel Cells
- 1.3 Properties of ORR Catalyst
- 1.4 Perovskites
- 1.5 The LaFeO₃ Perovskite

Chapter 2: Theory, Methodology and Computational Details

- 2.1 Density Functional Theory
 - 2.1.1 Many-body Schrödinger equation
 - 2.1.2 Clamped Nuclei Approximation
 - 2.1.3 Independent Electrons Approximation
 - 2.1.4 Exclusion Principle
 - 2.1.5 Mean-Field Approximation
 - 2.1.6 Hartree-Fock Equations
 - 2.1.7 Kohn-Sham Equations
 - 2.1.8 The Local Density Approximation
 - 2.1.9 Self-Consistent Calculations
- 2.2 Vienna Ab-initio Simulation Package (VASP)
- 2.3 Computational Modelling
- 2.4 Oxygen Reduction Reaction

2.5 Equations for Energy Calculation and Thermodynamic Analysis

Chapter 3: Results and Discussion

3.1 Equilibrium properties of bulk and 2D monolayer of LaFeO_3

3.2 Associative Mechanism of ORR

3.3 Dissociative Mechanism of ORR

3.4 Theoretical Overpotential Calculations

3.5 Spin Density Calculations

Chapter 4: Conclusions and Scope for Future Work

4.1 Conclusions

4.2 Scope for Future Work

REFERENCES

LIST OF FIGURES

Figure 1: ORR volcano plot for metal catalysts

Figure 2: Schematic of a Proton Exchange Membrane Fuel Cell (PEMFC).

Figure 3: A schematic of the crystal structure of a cubic perovskite oxide of the form ABO_3

Figure 4: Crystal structure of the $LaFeO_3$ perovskite.

Figure 5: Schematic flow-chart for finding self-consistent solutions of the Kohn-Sham equations.

Figure 6: Sample INCAR file of VASP

Figure 7: Sample POSCAR file of VASP.

Figure 8: Snippet of the POTCAR file of VASP

Figure 9: Sample KPOINTS file of VASP.

Figure 10: Snippet of the CONTCAR file of VASP.

Figure 11: Snippet of the CHGCAR file of VASP.

Figure 12: Visualization of the CHGCAR file of VASP.

Figure 13: Reaction pathway of (a) Associative mechanism, and (b) Dissociative mechanism of ORR.

Figure 14: (a) Equilibrium crystal structure, (b) electronic band structure, and (c) total density of states (DOS) of the 3D $LaFeO_3$ perovskite.

Figure 15: (a) Top and side view of the equilibrium crystal structure of 2D monolayer $LaFeO_3$, (b) electronic band structure, and (c) total DOSs of 2D monolayer $LaFeO_3$

Figure 16: Proposed four-electron associative and dissociative mechanism on the surface of 2D monolayer of the $LaFeO_3$ perovskite.

Figure 17: Schematic representation of (a) associative mechanism and (b) dissociative mechanism of the oxygen reduction reaction pathway performed on the surface of 2D monolayer $LaFeO_3$

Figure 18: (a) equilibrium structure, (b) band structure, and (c) total DOS of $\text{O}_2^*_{\text{-LaFeO}_3}$

Figure 19: (a) Equilibrium structure, (b) band structure, and (c) total DOS of $\text{OOH}^*_{\text{-LaFeO}_3}$

Figure 20: (a) Equilibrium structure, (b) band structure, and (c) total DOS of $\text{O}^*_{\text{-LaFeO}_3}$

Figure 21: (a) Equilibrium structure, (b) band structure, and (c) total DOS of $\text{OH}^*_{\text{-LaFeO}_3}$

Figure 22: (a) Equilibrium structure, (b) band structure, and (c) total DOS of $2\text{O}^*_{\text{-LaFeO}_3}$

Figure 23: O_2 dissociation of LaFeO_3 monolayer.

Figure 24: (a) Equilibrium structure, (b) band structure, and (c) total DOS of $\text{O}^*_{\text{-OH}^*_{\text{-LaFeO}_3}}$

Figure 25: Potential Energy Surface (PES) of the Associative ORR mechanism

Figure 26: Potential Energy Surface (PES) of the Dissociative ORR mechanism

LIST OF TABLES

Table 1: Equilibrium lattice constants of the 3D LaFeO₃ crystal structure

Table 2: Change in Gibbs Free Energy (eV) and the Relative Free Energy (eV) of each reaction step during the reduction of oxygen through the Associative Mechanism on the surface of the 2D monolayer LaFeO₃ materials

Table 3: Change in Gibbs Free Energy (eV) and the Relative Free Energy (eV) of each reaction step during the reduction of oxygen through the Dissociative Mechanism on the surface of the 2D monolayer LaFeO₃ material

Table 4: Geometrical data of the equilibrium structures of all the reaction intermediates involved in the Associative and the Dissociative Mechanisms on the surface of the 2D monolayer of the LaFeO₃ perovskite material.

ACRONYMS

ORR: Oxygen Reduction Reaction

PEMFCs: Proton Exchange Membrane Fuel Cells

MABs: Metal Air Batteries

RHE: Reversible Hydrogen Electrode

CHE: Computational Hydrogen Electrode

PEM: Proton Exchange Membrane

MEA: Metal Electrode Assembly

TPB: Triple Phase Boundary

HOR: Hydrogen Oxidation Reaction

SHE: Standard Hydrogen Electrode

FM: Ferromagnetic

AFM: Anti-Ferromagnetic

DFT: Density Functional Theory

HEG: Homogeneous Electron Gas

LDA: Local Density Approximation

DOS: Density Of States

HF: Hartree Fock

VASP: Vienna Ab-Initio Simulation Package

PAW: Projector Augmented Wave

FFT: Fast Fourier Transform

PBE: Perdew-Burke-Ernzerhof

GGA: Generalized Gradient Approximation

RMM-DIIS: Residual Minimization Method with Direct Inversion in the Iterative Subspace

CI-NEB: Climbing Image Nudged Elastic Band

TMDs: Transition Metal Dichalcogenides

Chapter 1

Introduction

1.1 Motivation

The world today is rapidly transforming into a global community, largely driven by the escalating demand for energy from all corners of the globe.^{1,2} However, the Earth itself remains unchanged in its capacity to provide this vital resource. The need for energy and its associated services to support human societal, economic, and health advancements is on the rise. Every society relies on energy services to fulfill fundamental human requirements like healthcare, illumination, cooking, environmental comfort, transportation, and communication, thereby facilitating generative processes. In this rapidly advancing world, meeting the increasing daily energy demands has led to the escalation of consumption of fossil fuels and this has become a significant concern due to its detrimental effects on the environment.³ This soaring demand has presented a dual challenge: securing energy supply and mitigating its impact to climate change. The prevalence of fossil fuel-driven electricity generation, including coal, oil, and gas, coupled with a significant population surge over recent decades, has created a surge in energy demand. Consequently, this surge has precipitated global challenges, primarily stemming from the rapid escalation of carbon dioxide (CO₂) emissions. Currently, 1.4 billion people have no access to electricity, with 85% of them residing in rural regions. This has resulted in an increase in rural communities depending upon traditional biomass use, expected to reach 2.8 billion by 2030 from 2.7 billion today.^{1,4,5} Thus, transitioning to alternative green energy sources is crucial for a greener future. Proton exchange membrane fuel cells (PEMFCs) and metal-air batteries (MABs) among other conventional sources of energy, stand out as promising solutions. Fuel cells are electrochemical devices that take hydrogen as fuel and give out water, electricity, and some heat as the only by-products.⁶ The invention of these cells is credited to Sir William Grove in the middle 19th century, and they serve as an advantage due to their high efficiency and potential for zero carbon emissions.

During the discharging phase of fuel cells, the reduction of oxygen by electrons takes place at the cathode or the oxygen reduction side. ORR can occur either through a four-electron or a two-electron reduction pathway resulting in H₂O and H₂O₂ as a product respectively. The four-electron reduction pathway is thermodynamically favorable due to lower equilibrium potential (1.23V vs RHE) as compared to the two-electron pathway (0.70V vs RHE).⁷ The prime obstacle in fuel cells is the sluggish kinetics and high overpotential of the oxygen reduction reaction. To eliminate this hindrance in the efficiency of these cells and to speed up the ORR kinetics, the assistance of highly active, stable, and economical electrocatalysts is imperative. Typically, the cathode requires ten times the amount of catalyst as compared to the anode.⁸ Platinum-based materials have low overpotential and are industrially used as a stable and highly active

electrocatalyst for oxygen reduction in acidic medium whereas Palladium (Pd) is the alkaline counterpart. However, like most noble metals, Pt and Pd suffer critical challenges regarding economic affordability and stability upon contamination. Different other noble metals, such as Pd, Ir, Cu, Ag, Ir, Co and Ru have been employed as cathode materials for reduction of oxygen. The order of electrocatalytic activity of these noble metals for ORR is as follows: Pt > Pd > Ir > Rh.⁹ According to previous studies, Ru can undergo a four-electron reduction.¹⁰ While Ag is not so efficient for ORR in comparison to platinum, it exhibits greater stability than Pt cathodes during prolonged operations.¹¹ The ORR activity trend in these metals among others is illustrated in Figure 1 by the volcano plot which depicts the activities of these catalysts as a function of their binding energy.¹²

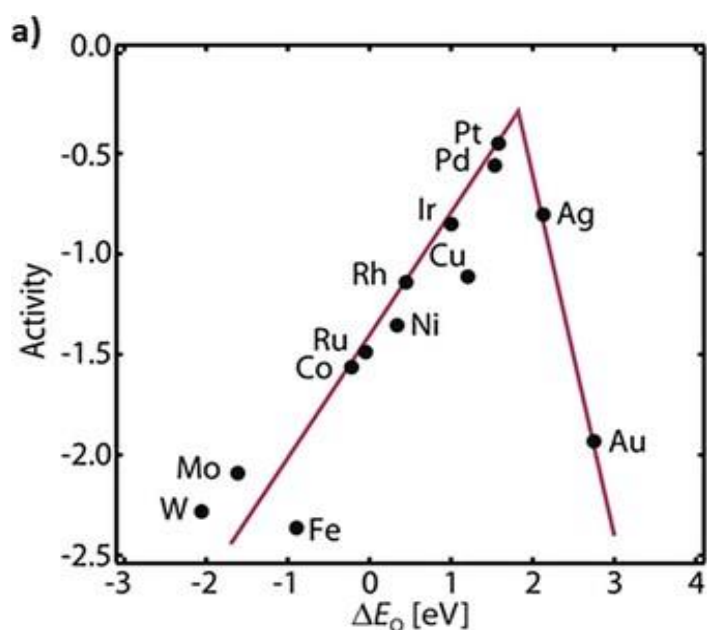


Figure 1: ORR volcano plot for metal catalysts

Thus, there is a need to search for alternative electrocatalysts to expensive Pt to be used as a catalyst to reduce oxygen in an environmentally friendly manner. Hence, our motivation lies in developing novel materials to speed up the sluggish ORR kinetics at the cathode of fuel cells.¹³

1.2 Fuel Cells

A fuel cell is an electrochemical cell that transforms the chemical energy of a fuel (typically hydrogen) and an oxidizing agent (typically oxygen) into electricity through a series of redox reactions.¹⁴ Fuel cells are of advantage over most batteries since fuel cells utilize oxygen from the air to keep the chemical reaction going whereas batteries use chemical energy from the substances present in the battery itself. In addition to this, fuel cells can continuously generate electricity for as long as there is a sufficient supply of oxygen and fuel. They are utilized for providing primary and backup power for various applications including commercial, industrial, and residential buildings, as well as in remote areas.

The general configuration of a fuel cell includes an anode, a cathode, and an electrolyte. Fuel cells can be categorized into various types based on the type of electrolyte utilized. One of these is the proton exchange membrane fuel cell (PEMFC), which is also known as the polymer electrolyte membrane (PEM) fuel cell. These PEMFCs are constructed using membrane electrode assemblies (MEAs) which include electrodes (anode and cathode); an electrolyte substance which may be made up of several substances like potassium hydroxide, salt carbonates, and phosphoric acid; anode and cathode catalysts which help to break down the fuel into electrons and ions at the anode and convert ions into required by products and water vapor at the cathode; and gas diffusion layers that prevent oxidization. This fuel cell takes hydrogen as a fuel from the anode side where the hydrogen atom splits into a proton (H^+) and an electron (e^-). The H^+ ions then penetrate through the proton exchange membrane and reach the cathode side, whereas the electrons reach the cathode via the external circuit producing direct current and reach the ORR side of the fuel cell. At the cathode, a catalyst causes the ions, electrons, and oxygen from the air to react and produce water and other by-products such as heat. A schematic of the proton exchange membrane fuel cell is represented in Figure 2. The critical component of the cell is the triple phase boundary (TPB) where the electrolyte, catalyst, and reactants mix with each other thereby facilitating the cell reactions. Typically, the energy efficiency of a fuel cell ranges between 40% and 60%; however, by capturing waste heat in a cogeneration scheme, efficiencies of up to 85% can be achieved.

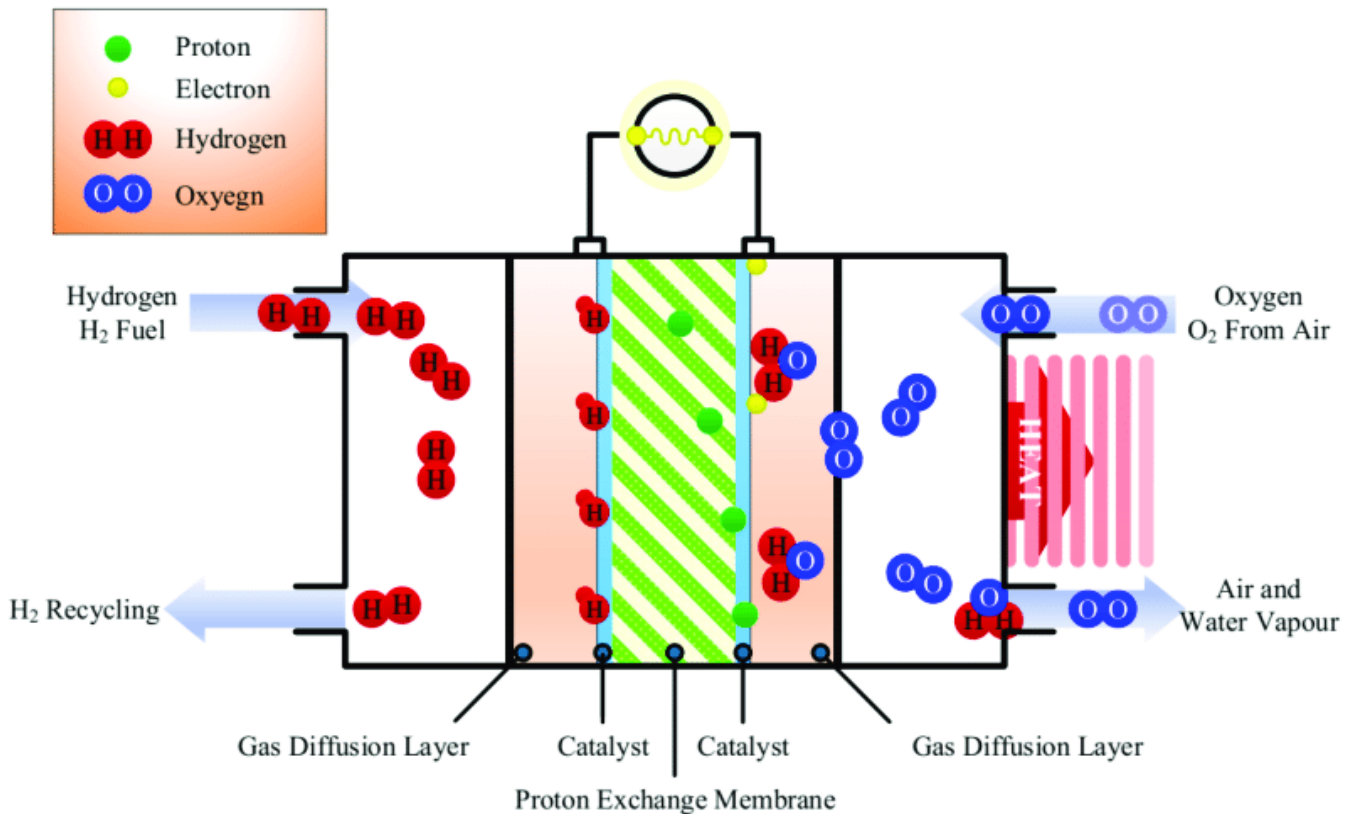


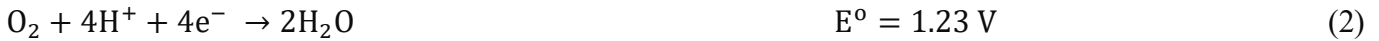
Figure 2: Schematic of a Proton Exchange Membrane Fuel Cell (PEMFC).

The oxidation half-cell reaction or the hydrogen oxidation reaction is given by:



The electrons that reach the cathode side through the external circuit react with the H^+ ions that penetrate across the polymer electrolyte membrane and the oxygen molecules from the air to finally produce water molecules.

The reduction half-cell reaction or ORR is given by:



The overall reaction is given by:



In each case, the potentials are referenced with respect to the standard hydrogen electrode (SHE).

1.3 Properties of ORR Catalyst

Over the past two decades, a multitude of ORR electrocatalysts have been explored. However, meeting the following criteria is crucial for ensuring the effectiveness of an ORR electrocatalyst:

1. High catalytic activity towards ORR.
2. High electrical conductivity.
3. High chemical and electrochemical stability, ensuring resistance to oxidation by protons or oxygen, even at high electrode potentials.
4. It should not be insolubility in the electrolyte and must remain stable in acidic, basic solutions or in methanolic solutions.
5. Favorable structural composition and morphology, specific surface area, porosity, particle size, and even distribution of catalyst particles on the support.
6. Strong interaction between the catalyst particles and the support surface.
7. Long-term electrocatalytic stability, which can be compromised if any of the requirements are not met.

1.4 Perovskites

In the recent past, there have been extensive studies on alternative ORR catalysts and these findings have suggested that transition-metal oxides and in particular, perovskite oxides having the structure ABO_3 exhibit promising catalytic properties for ORR in alkaline fuel cells and MABs. Perovskites are calcium titanium oxide minerals that are composed of CaTiO_3 . These minerals are found in the earth's mantle and were first discovered by Gustav Rose in Russia in the year 1839. The term "perovskite" was coined after the Russian mineralogist L.A. Perovski and this term is not only used to refer to the mineral

CaTiO₃ but also extends to a group of compounds that have the same crystal structure. This structure, is called the perovskite structure, is characterized by the general chemical formula ABX₃ where ‘A’ and ‘B’ are two cations where ‘A’ atoms are usually bigger than the ‘B’ atoms and ‘X’ is typically a negatively charged ion, i.e., an anion which is generally an oxide that bonds to both the cations. The ideal crystal structure of a perovskite is cubic, where the B cation (usually a transition metal) exhibits a 6-fold coordination and sits at the body-center (1/2, 1/2, 1/2) surrounded by an octahedron of anions. The A cation has a 12-fold cuboctahedral coordination and is situated at the corner position (0, 0, 0) of the cube. The anions, typically oxygen atoms occupy the face-centered positions (1/2, 1/2, 0), (1/2, 0, 1/2), and (0, 1/2, 1/2). A schematic representation of the structure of a cubic perovskite is depicted in Figure 3. This structure allows for the incorporation of various cations, leading to the creation of a wide range of engineered materials with diverse properties.

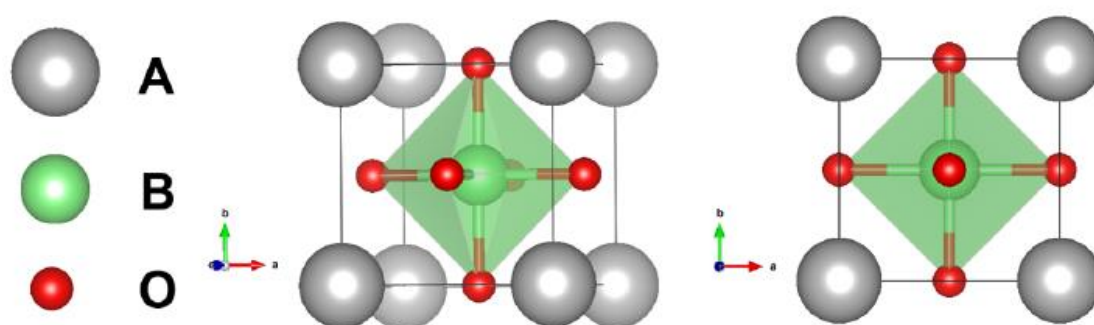


Figure 3: A schematic representation of the crystal structure of a cubic perovskite oxide (ABO₃)

These perovskite oxides have flexible and tunable electronic and physical/chemical properties. In addition to this, they have a low cost and are environmentally friendly. Due to their wide range of properties, perovskites find applications in photovoltaics, lasers, light-emitting diodes (LEDs), photoelectrolysis, and scintillators. Along with these advantages, comes a notable challenge of relatively low electrical conductivity which hinders fast charge transfer and leads to an increased overpotential. Various approaches that can be implemented to tackle this problem include defect introduction, doping various metals to either the A-site or B-site, strain tuning and the addition of carbon to enhance electrical conductivity. Since the 1970s, Lanthanum-based (La-based) perovskites have demonstrated impressive electrocatalytic activity towards ORR in alkaline media due to their high abundance, impressive qualities, and versatility.¹⁵ Several La-based perovskite oxides have been investigated, including LaBO₃ (B = Co, Mn, Ni, Cr) and they show high electrocatalytic activity for ORR to be utilized in fuel cells in alkaline media.^{16,17} Among other transition metal perovskite oxides, LaFeO₃ displays high stability in both oxidizing and reducing atmospheres. It also exhibits decent ionic and electronic conductivities that can be boosted through doping. These properties make LaFeO₃ a prime candidate for fuel cell applications.

1.5 The LaFeO₃ Perovskite

Perovskites, in general, demonstrate favorable catalytic properties and offer cost advantages as well as superior thermal resistivity as compared to noble metals. Perovskites with the composition ABO₃, where A and B are represented by La and Mn, Co, Fe, or Cr, respectively exhibit exceptional catalytic properties, particularly in oxidation processes.¹⁸ When considering AFeO₃ perovskites, where A represents La, Sm, or Nd, synthesized through the citrate method, the methane oxidation activity of these perovskites can be ranked as follows: LaFeO₃ > NdFeO₃ > SmFeO₃.^{19,20} The LaFeO₃ perovskite demonstrates reduced activity in the aforementioned processes, however it has a high thermal resistance. LaFeO₃ possesses a cubic perovskite structure, characterized by the space group $Pm\bar{3}m$. The crystal structure of the LaFeO₃ perovskite is shown in Figure 4.

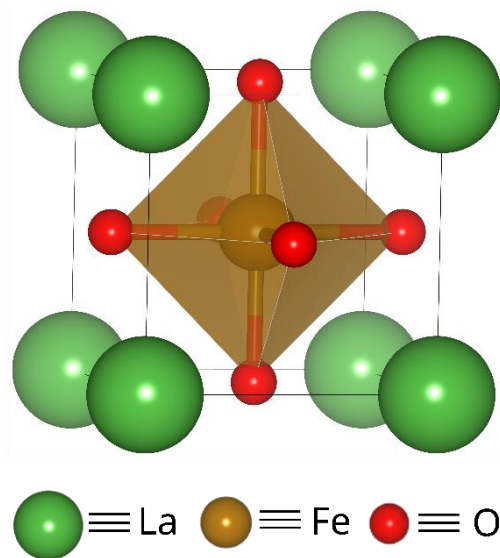


Figure 4: Crystal structure of the LaFeO₃ perovskite.

In this structure, La sits at the corner positions, Fe at the body center, and O atoms at the face centers of the unit cell. Notably, with a Neel temperature of 740 K, bulk LaFeO₃ exhibits antiferromagnetic properties. Its remarkable mixed conductivity makes it a promising material for electro-ceramic applications. LaFeO₃ demonstrates chemical stability in both reducing and oxidizing environments. Through atomic doping, LaFeO₃ can exhibit improved properties for example enhanced electrical conductivity, reduced dielectric loss susceptibility, larger dielectric constant increased polarizability, and a shift in the average type of permittivity. Various synthesis methods have been developed for the fabrication of LaFeO₃. Various magnetic arrangements are possible for the Fe³⁺ ions within the LaFeO₃ lattice: ferromagnetic (FM), where the magnetic dipoles of all Fe³⁺ ions are aligned, and antiferromagnetic (AFM), where the magnetic moments of neighboring Fe³⁺ ions are in opposite directions.

Chapter 2

Theory, Methodology, and Computational Details

2.1 Density Functional Theory (DFT) Methods

‘Materials modeling’ refers to the development and application of mathematical models to describe and predict specific properties of materials at a quantitative level.²¹ When it is indicated that a model is "from first principles," or alternatively, when it is mentioned that an ab initio model is employed, it points towards the usage of a bottom-up modeling strategy, as opposed to a top-down approach. In today’s world, the computational modeling of materials employing first principles relies on a range of theoretical and computational techniques. The common principle of these methods is their reliance upon density functional theory, traditionally shortened as ‘DFT’. From a practical standpoint, Density Functional Theory proves to be highly effective for investigating nanostructures, molecules, surfaces, solids, and interfaces. It achieves this by solving an approximate version of the Schrödinger equation. A few key strengths of DFT include its transferability of methods, simplicity, reliability, and software sharing. Limitations of the theory include inaccuracies in describing the van der Waals binding of biological molecules, red-shifted optical absorption spectra, and occasional mispredictions of metallic properties in transition metal oxides.

When modeling solid-state systems, it is essential to define two structures: The unit cell in real space is characterized by lattice parameters a , b , and c , along with the angles α , β , and γ . Extending the unit cell infinitely in each lattice parameter direction results in the formation of the crystal structure. Reciprocal space is constructed similarly, with a series of Wigner-Seitz cells forming it. A single Wigner-Seitz cell is commonly known as the first Brillouin zone. A reciprocal lattice vector can be expressed as:

$$\mathbf{G} = 2\pi n\mathbf{a}^* + 2\pi m\mathbf{b}^* + 2\pi c^* \quad (4)$$

The function $e^{i\mathbf{G}\cdot\mathbf{r}}$ oscillates with the same periodicity as the real space lattice. Therefore, when a function is expressed as a Fourier series of $e^{i\mathbf{G}\cdot\mathbf{r}}$, the resulting series inherits the periodicity of the real lattice. This attribute of the reciprocal lattice vectors is important when plane waves are considered.

2.1.1 Many-body Schrödinger equation

At the atomic scale, materials are collections of electrons and nuclei, i.e.,

$$\text{Materials} = \text{electrons} + \text{nuclei}$$

When considering the collective behavior of many electrons and nuclei, it becomes necessary to introduce a many-body wavefunction, denoted as Ψ . This wavefunction is dependent on the positions of each electron and nucleus within the system. For a system containing N electrons, having coordinates $\mathbf{r}_1, \mathbf{r}_2, \dots, \mathbf{r}_N$ and M nuclei having coordinates $\mathbf{R}_1, \mathbf{R}_2, \dots, \mathbf{R}_M$ the many-body wavefunction can be represented as:

$$\Psi = \Psi(\mathbf{r}_1, \mathbf{r}_2, \dots, \mathbf{r}_N; \mathbf{R}_1, \mathbf{R}_2, \dots, \mathbf{R}_M) \quad (5)$$

The term $|\Psi(\mathbf{r}_1, \mathbf{r}_2, \dots, \mathbf{r}_N; \mathbf{R}_1, \mathbf{R}_2, \dots, \mathbf{R}_M)|^2$ gives the probability to find simultaneously the first electron at point r_1 , the second electron at point r_2 , and so on, while the nuclei are at positions $\mathbf{R}_1, \mathbf{R}_2, \dots, \mathbf{R}_M$ and so forth. The time-independent Schrödinger equation for a many-body system can be written as follows:

$$(\text{kinetic energy} + \text{potential energy})\Psi = E_{tot}\Psi \quad (6)$$

Where, E_{tot} , is the eigenvalue and represents the total energy of the system in the quantum state which is specified by the many-body wavefunction Ψ . Considering N electrons and M nuclei, the kinetic energy term can be written as:

$$\text{kinetic energy} = -\sum_{i=1}^N \frac{\hbar^2}{2m_e} \nabla_i^2 - \sum_{I=1}^M \frac{\hbar^2}{2M_I} \nabla_I^2 \quad (7)$$

Where the masses of nuclei are M_1, M_2, \dots are and m_1, m_2, \dots are the masses of electrons in the system. For potential energy term, we will have to take into account all the pairs of charges in the many-body system. Firstly, taking into account the Coulomb repulsion between electron pairs:

$$(\text{potential energy})_{ee} = \frac{1}{2} \sum_{i \neq j} \frac{e^2}{4\pi\epsilon_0} \frac{1}{|\mathbf{r}_i - \mathbf{r}_j|} \quad (8)$$

Here the indices j and i run range 1 to N . Those terms having $i = j$ have not been considered because an electron does not repel itself, and we divide by 2 in order to count only one contribution per pair. Second, we have the Coulomb repulsion between pairs of nuclei:

$$(\text{potential energy})_{nn} = \frac{1}{2} \sum_{I \neq J} \frac{e^2}{4\pi\epsilon_0} \frac{Z_I Z_J}{|\mathbf{R}_I - \mathbf{R}_J|} \quad (9)$$

Here, the indices I and J range from 1 to M, with Z_I representing the atomic numbers. Additionally, we consider the Coulomb attraction between electrons and nuclei.

$$(\text{potential energy})_{en} = -\sum_{i,I} \frac{e^2}{4\pi\epsilon_0} \frac{Z_I}{|r_i - R_I|} \quad (10)$$

with i ranging from 1 to N, and I ranging from 1 to M.

Simplifying these terms using the Hartree atomic units, the new form of the many-body Schrödinger equation can be written as:

$$\left[-\sum_i \frac{\nabla_i^2}{2} - \sum_I \frac{\nabla_I^2}{2M_I} - \sum_{i,I} \frac{Z_I}{|r_i - R_I|} + \frac{1}{2} \sum_{i \neq j} \frac{1}{|r_i - r_j|} + \frac{1}{2} \sum_{I \neq J} \frac{Z_I Z_J}{|R_I - R_J|} \right] \Psi = E_{tot} \Psi \quad (11)$$

This is the most frequently employed formulation of the many-body Schrödinger equation in first-principles materials modelling. This equation notably illustrates that the only external parameters required in this approach are the atomic numbers, Z_I , and the atomic masses, M_I .

2.1.2 Clamped Nuclei Approximation

The many-body Schrödinger equation represented in equation 11 will be immensely complicated since it is too general and caters to every phase ranging from gases, to liquids to solids. Now, it is appropriate to narrow down and consider only molecules and solid. In investigations involving gases, liquids, and plasmas, nuclei often traverse considerable distances. Conversely, in the context of solids and molecules adsorbed on solid surfaces, nuclei typically remain stationary or in close proximity to a specific position. Thus, here we make an assumption and consider the nuclei to be immobile or clamped in known positions. Therefore, here we consider that the nuclei cannot move and have infinite mass ($M_I = \infty$). This consideration leads us to disregard the kinetic energy of the nuclei in equation 11 and treat the Coulomb repulsion between nuclei as a constant. For simplicity, we move this constant to the right-hand side of equation 11 by defining:

$$E = E_{tot} - \frac{1}{2} \sum_{I \neq J} \frac{Z_I Z_J}{|R_I - R_J|} \quad (12)$$

Since we are considering nuclei to be clamped at certain positions, we can neglect the nuclear coordinates and consider the many-body wavefunction Ψ to be a function of electronic coordinates only, i.e., $\Psi = \Psi(r_1, r_2, \dots, r_N)$. In addition to this, Coulomb potential experienced by the electrons due to the presence of nuclei can be defined as:

$$V_n(r) = -\sum_I \frac{Z_I}{|r - R_I|} \quad (13)$$

Using the above approximations and definitions, equation 11 can be rewritten as:

$$\left[-\sum_i \frac{\nabla_i^2}{2} + \sum_i V_n(\mathbf{r}_i) + \frac{1}{2} \sum_{i \neq j} \frac{1}{|\mathbf{r}_i - \mathbf{r}_j|} \right] \Psi = E \Psi \quad (14)$$

This represents the fundamental equation of the electronic structure theory. Now, we define the many-electron Hamiltonian:

$$\hat{H}(\mathbf{r}_1, \dots, \mathbf{r}_N) = -\sum_i \frac{\nabla_i^2}{2} + \sum_i V_n(\mathbf{r}_i) + \frac{1}{2} \sum_{i \neq j} \frac{1}{|\mathbf{r}_i - \mathbf{r}_j|} \quad (15)$$

Now, equation 14 can be written compactly as:

$$\hat{H} \Psi = E \Psi \quad (16)$$

Additionally, from equation 15 we can define the single-electron Hamiltonian:

$$\hat{H}_0(\mathbf{r}) = -\frac{1}{2} \nabla^2 + V_n(\mathbf{r}) \quad (17)$$

Now, we split the many-electron Hamiltonian and reach at the following form:

$$\hat{H}(\mathbf{r}_1, \dots, \mathbf{r}_N) = \sum_i \hat{H}_0(\mathbf{r}_i) + \frac{1}{2} \sum_{i \neq j} \frac{1}{|\mathbf{r}_i - \mathbf{r}_j|} \quad (18)$$

2.1.3 Independent electrons approximation

In order to solve equation 14, we need to simplify it further and we do this by eliminating the term that describes the Coulomb repulsion between electrons from equation 14. This is performed because this term constitutes the only mode of interaction between the electrons. Without it, the electrons would not perceive each other. This approximation is known as the ‘independent electron approximation’. Using equations 16 and 18 the Schrödinger equation within the independent electron approximation becomes:

$$\sum_i \hat{H}_0(\mathbf{r}_i) \Psi = E \Psi \quad (19)$$

Now, we can write the many-body wavefunction (the solution of equation 19) as a product of the single-electron wavefunctions:

$$\Psi(\mathbf{r}_1, \mathbf{r}_2, \dots, \mathbf{r}_N) = \varphi_1(\mathbf{r}_1) \dots \varphi_N(\mathbf{r}_N) \quad (20)$$

The single electron Schrödinger equation within the independent electron approximation becomes:

$$\hat{H}_0(\mathbf{r}) \varphi_i(\mathbf{r}) = \varepsilon_i \varphi_i(\mathbf{r}) \quad (21)$$

The aforementioned equation embodies the independent electron approximation, yet it harbors two drawbacks. The first pertains to its failure to adhere to the Pauli exclusion principle, which dictates that the wavefunction should change sign whenever the positions and spins of any two electrons are exchanged. Secondly, the Coulomb term cannot be eliminated since all other terms in the equation have the same magnitude. These issues have been addressed in the upcoming sections.

2.1.4 Exclusion principle

The wavefunction given by equation 20 fails to obey the Pauli exclusion principle but the following fulfills this shortcoming:

$$\Psi(\mathbf{r}_1, \mathbf{r}_2) = \frac{1}{\sqrt{2}} [\varphi_1(\mathbf{r}_1)\varphi_2(\mathbf{r}_2) - \varphi_1(\mathbf{r}_2)\varphi_2(\mathbf{r}_1)] \quad (22)$$

By direct substitution, we find that $\Psi(\mathbf{r}_2, \mathbf{r}_1) = -\Psi(\mathbf{r}_1, \mathbf{r}_2)$. Moreover, each of the terms on the right-hand side of equation 22 contributes to the total energy, represented as $E = \varepsilon_1 + \varepsilon_2$ when replaced in equation 19. Equation 22 can be written in a compact form by using a matrix determinant of the following form:

$$\Psi(\mathbf{r}_1, \mathbf{r}_2) = \frac{1}{\sqrt{2}} \begin{vmatrix} \varphi_1(\mathbf{r}_1) & \varphi_1(\mathbf{r}_2) \\ \varphi_2(\mathbf{r}_1) & \varphi_2(\mathbf{r}_2) \end{vmatrix} \quad (23)$$

This is referred to as the Slater determinant. For constructing a Slater determinant with N electrons, the prefactor becomes $N!^{-1/2}$ (for $N > 2$) instead of $2^{-1/2}$. Consequently, the electron charge density is computed by summing up the probabilities of finding electrons in each of the occupied state i:

$$n(\mathbf{r}) = \sum_i |\phi_i(\mathbf{r})|^2 \quad (24)$$

2.1.5 Mean-field approximation

According to classical electrostatics, an electronic charge distribution, $n(\mathbf{r})$, generates an electrostatic potential $\varphi(\mathbf{r})$ through Poisson's equation:

$$\nabla^2 \varphi(\mathbf{r}) = 4\pi n(\mathbf{r}) \quad (25)$$

The electrons that are immersed in this electrostatic potential have a potential energy $V_H(\mathbf{r}) = -\varphi(\mathbf{r})$. This potential that is represented in the Hartree units is called the 'Hartree potential'. This Hartree potential satisfies the Poisson's equation as:

$$\nabla^2 V_H(\mathbf{r}) = -4\pi n(\mathbf{r}) \quad (26)$$

The solution to the above equation is:

$$V_H(\mathbf{r}) = \int d\mathbf{r}' \frac{n(\mathbf{r}')}{|\mathbf{r}-\mathbf{r}'|} \quad (27)$$

Since this Hartree potential is experienced by every electron in the system, we can improve equation 21 by considering this extra term:

$$\left[-\frac{\nabla^2}{2} + V_n(\mathbf{r}) + V_H(\mathbf{r})\right] \varphi_i(\mathbf{r}) = \varepsilon_i \varphi_i(\mathbf{r}) \quad (28)$$

$$n(\mathbf{r}) = \sum_i |\varphi_i(\mathbf{r})|^2 \quad (29)$$

$$\nabla^2 V_H(\mathbf{r}) = -4\pi n(\mathbf{r}) \quad (30)$$

Here, since V_H is the ‘average’ potential experienced by each electron, this approach is called as the mean-field approximation. Equations 28 to 30 must be solved simultaneously. This means that the solutions φ_i obtained from equation 28 must be such that, when used to calculate the Hartree potential V_H according to equations 29 and 30, the resulting potential when substituted back into equation 28, reproduces the same solutions φ_i . This iterative process is known as a self-consistent field method, pioneered by Hartree in 1928, therefore the subscript ‘H’ in the potential.

2.1.6 Hartree-Fock equations

The Hartree-Fock equations are given by:

$$\left[-\frac{\nabla^2}{2} + V_n(\mathbf{r}) + V_H(\mathbf{r})\right] \varphi_i(\mathbf{r}) + \int d\mathbf{r}' V_X(\mathbf{r}, \mathbf{r}') \varphi_i(\mathbf{r}') = \varepsilon_i \varphi_i(\mathbf{r}) \quad (31)$$

$$n(\mathbf{r}) = \sum_i |\varphi_i(\mathbf{r})|^2 \quad (32)$$

$$\nabla^2 V_H(\mathbf{r}) = -4\pi n(\mathbf{r}) \quad (33)$$

Where V_X is known as the Fock exchange potential and is given by:

$$V_X(\mathbf{r}, \mathbf{r}') = -\sum_j \frac{\varphi_j^*(\mathbf{r}') \varphi_j(\mathbf{r})}{|\mathbf{r}-\mathbf{r}'|} \quad (34)$$

where the summation is performed over the occupied single-particle states. V_X primarily arises from Pauli’s exclusion principle and prohibits two electrons from occupying the same quantum state.

2.1.7 Kohn-Sham equations

The Kohn-Sham equation is given by:

$$\left[-\frac{\nabla^2}{2} + V_n(\mathbf{r}) + V_H(\mathbf{r}) + V_x(\mathbf{r}) + V_c(\mathbf{r}) \right] \varphi_i(\mathbf{r}) = \varepsilon_i \varphi_i(\mathbf{r}) \quad (35)$$

Here another term $V_c(\mathbf{r})$ has been added where ‘c’ stands for correlation. The exchange potential V_x has been replaced by a simpler version $V_x(\mathbf{r})$ which is called the local exchange potential. The fundamental concept of density functional theory posits that if E represents the lowest attainable energy of the system, i.e., the energy of the ground state, then E is a functional solely dependent on the electron density. This can be expressed as follows:

$$E = F[n] \quad (36)$$

The above equation represents the Hohenberg-Kohn theorem, which suggests that to calculate the energy of the ground state, we just need the electron density, n . While for the energy calculation of excited states, we require the complete many-body wavefunction Ψ . The kinetic energy and the Coulomb energy are given as follows:

$$\hat{T} = \sum_i \frac{1}{2} \nabla_i^2 \quad (37)$$

$$\hat{W} = \frac{1}{2} \sum_{i \neq j} \frac{1}{|r_i - r_j|} \quad (38)$$

The energy of the ground state that is a functional of the electron density only is then given by:

Total energy in the independent electrons approximation

$$E = F[n] = \underbrace{\int d\mathbf{r} n(\mathbf{r}) V_n(\mathbf{r})}_{\text{External potential}} - \underbrace{\sum_i \int d\mathbf{r} \varphi_i^*(\mathbf{r}) \frac{\nabla^2}{2} \varphi_i(\mathbf{r})}_{\text{Kinetic energy}} + \underbrace{\frac{1}{2} \iint d\mathbf{r} d\mathbf{r}' \frac{n(\mathbf{r})n(\mathbf{r}')}{|\mathbf{r}-\mathbf{r}'|}}_{\text{Hartree energy}} + \underbrace{E_{xc}[n]}_{\text{XC energy}} \quad (39)$$

E_{xc} is called the exchange and correlation energy which is unknown. The ground-state density n_0 minimizes the total energy, $E = F[n]$. This is known as the ‘Hohenberg-Kohn variational principle’ and is represented as:

$$\left. \frac{\delta F[n]}{\delta n} \right|_{n_0} = 0 \quad (40)$$

This principle leads to a newer version of the Kohn-Sham equation:

$$\left[-\frac{\nabla^2}{2} + V_n(\mathbf{r}) + V_H(\mathbf{r}) + V_{xc}(\mathbf{r}) \right] \varphi_i(\mathbf{r}) = \varepsilon_i \varphi_i(\mathbf{r}) \quad (41)$$

This set of equations are called the Kohn-Sham equations. Here, the extra term V_{xc} is given by:

$$V_{xc}(\mathbf{r}) = \left. \frac{\delta E_{xc}[n]}{\delta n} \right|_{n(\mathbf{r})}, \quad (42)$$

and this is known as the exchange and correlation potential. With the exact values of E_{xc} and V_{xc} , all the many-body effects can be considered. Hence, there must be a functional $E_{xc}[n]$ which gives the exact ground-state energy and density using the above equations 41 and 42. To know the exact value of this functional, we need to construct certain approximations, and these are discussed in the following sections.

2.1.8 The Local Density Approximation

Here, we introduce the simplest functional, known as the local density approximation to density functional theory. To examine this functional, we delve into the free homogeneous electron gas (HEG) model, where it is presumed that the electrons do not interact with each other, and N electrons are confined within a large box of volume V . With the assistance of this model, we can approximate the value of the exchange-correlation functional as follows:

$$dE_{xc} = \frac{E_{xc}^{HEG}[n(\mathbf{r})]}{V} d\mathbf{r} \quad (43)$$

This equation defines the LDA to the density functional theory, and thus the exchange energy for the entire system will be given by:

$$E_x = -\frac{3}{4} \left(\frac{3}{\pi} \right)^{1/3} \int n^{4/3}(\mathbf{r}) d\mathbf{r} \quad (44)$$

where the integration is performed over the volume V , and the exchange potential is given by:

$$V_x(\mathbf{r}) = \left. \frac{\delta E_x[n]}{\delta n} \right|_{n(\mathbf{r})} \quad (45)$$

2.1.9 Self-Consistent Calculations

The Kohn-Sham equations in summary are given as follows:

$$\left[-\frac{\nabla^2}{2} + V_{tot}(\mathbf{r})\right] \varphi_i(\mathbf{r}) = \varepsilon_i \varphi_i(\mathbf{r}) \quad (46)$$

$$V_{tot}(\mathbf{r}) = V_n(\mathbf{r}) + V_H(\mathbf{r}) + V_{xc}(\mathbf{r}) \quad (47)$$

$$V_n(r) = -\sum_l \frac{Z_l}{|r-R_l|} \quad (48)$$

$$\nabla^2 V_H(\mathbf{r}) = -4\pi n(\mathbf{r}) \quad (49)$$

$$V_{xc}(\mathbf{r}) = \frac{\delta E_{xc}[n]}{\delta n}(\mathbf{r}) \quad (50)$$

$$n(\mathbf{r}) = \sum_i |\varphi_i(\mathbf{r})|^2 \quad (51)$$

From these equations, we can observe that each solution φ_i is influenced by all other solutions φ_j which describe the occupied electronic states. The interdependence of all the solutions φ_i described in the above Kohn-Sham equations, equations 46 - 51, necessitates their determination through a self-consistent process. The practical approach to solving the Kohn-Sham equations is as follows: we begin by defining the nuclear coordinates, allowing us to compute the nuclear potential, V_n from equation 48. It is more pragmatic to "approximate" a potential electron density, $n(\mathbf{r})$, to establish an initial estimate for the Hartree, exchange, and correlation potentials to solve equation 46. Subsequently, we obtain the value for V_{tot} . By solving the Kohn-Sham equations, we derive new wavefunctions, φ_i , which can then aid in refining the density, n , and the total potential, V_{tot} . This iterative process persists until the updated density closely aligns with the previous one within a specified tolerance, signifying the achievement of self-consistency. This iterative procedure is depicted in Figure 5.

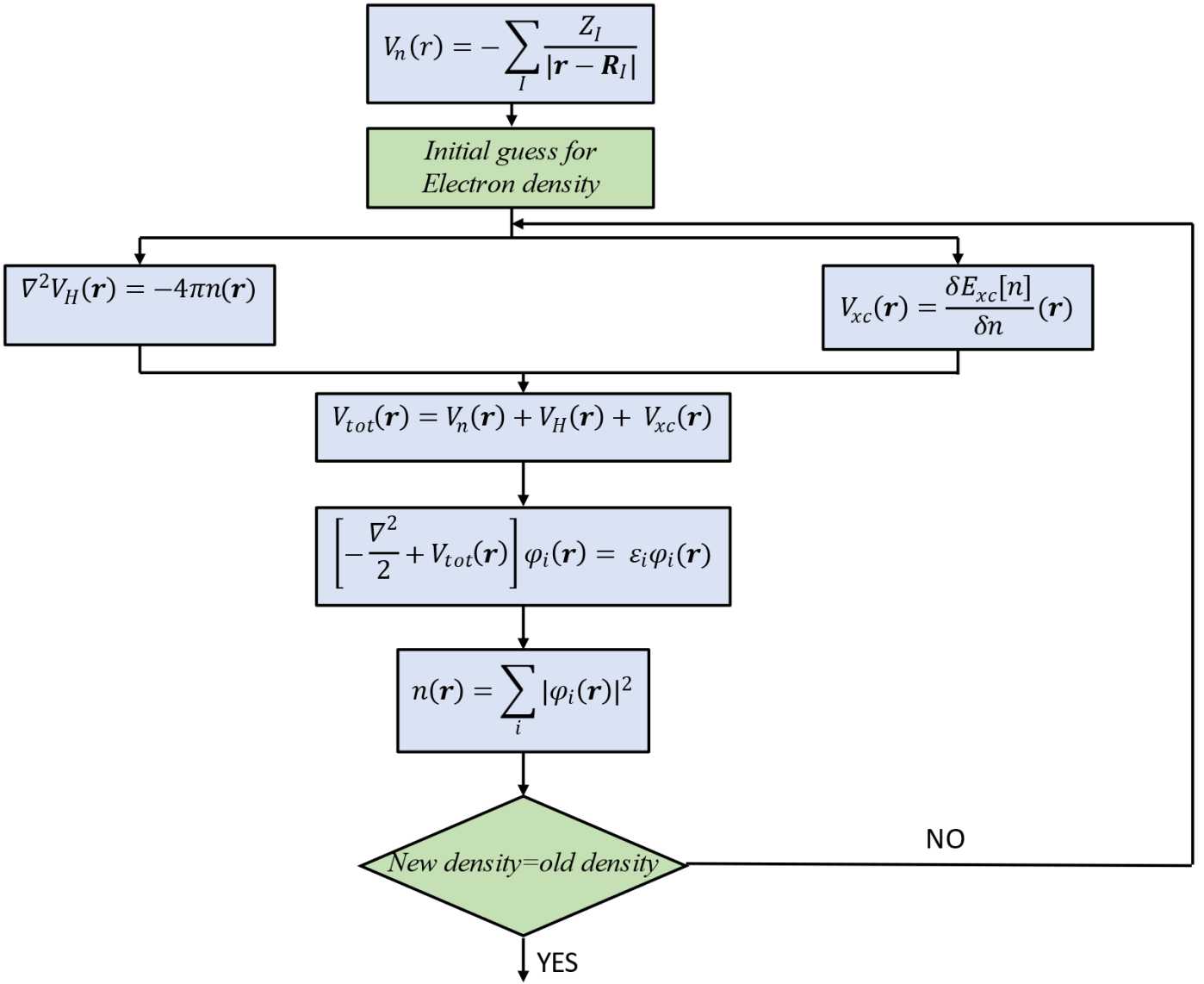


Figure 5: Schematic flow-chart for finding self-consistent solutions of the Kohn-Sham equations.

2.2 Vienna Ab-initio Simulation Package (VASP)

The Vienna Ab initio Simulation Package (VASP) is a software tool designed for atomic-scale materials modelling. It facilitates electronic structure calculations and quantum-mechanical molecular dynamics simulations based on first principles. VASP provides an approximate solution to the many-body Schrödinger equation, employing either density functional theory (DFT) to solve the Kohn-Sham equations or the Hartree-Fock (HF) approximation to solve the Roothaan equations. In VASP, fundamental quantities such as the one-electron orbitals, electronic charge density, and local potential are represented in plane wave basis sets. The interactions between electrons and ions are characterized using norm-conserving or ultrasoft pseudopotentials, or through the projector-augmented-wave method.

VASP requires the following input files:

1. INCAR

The INCAR file serves as the primary input file for VASP, dictating the actions and methodologies to be employed. The INCAR tags specified within the file select the algorithms and define the parameters utilized by VASP throughout the calculation process. A sample INCAR file used for the structure relaxation process of 2D monolayer LaFeO₃ has been presented in Figure 6. A short description of all the tags is given against each one of them.

```
# INCAR file for Structure Relaxation in VASP

# System Name
SYSTEM = 2D_LaFeO3

# Electronic Structure Method
GGA = PE # Generalized Gradient Approximation

# VASP 6.2.1 Settings
LREAL = .FALSE. # No real space projection; accurate but slower
PREC = Normal # Precision of calculation
NELM = 60 # Maximum number of SCF cycles
EDIFF = 1E-04 # Stopping criterion for energy convergence
ISMEAR = 0 # Smearing: 0 for crystals, -5 for insulators/semiconductors
ISPIN = 2 # Spin-polarized calculation
SIGMA = 0.05 # Smearing width
IALGO = 38 # Algorithm for electron optimization (usually most reliable)
ISTART = 0 # Start from scratch (wavecar not present)
ICHARG = 2 # Charge density included
LWAVE = .TRUE. # (Write WAVECAR or not)
LCHARG = .TRUE. # (Write CHGCAR or not)
ADDGRID = .TRUE. # (Increase grid, helps GGA convergence)

# Electronic Relaxation
ENCUT = 450.00 eV # Plane wave energy cutoff
ENAU = 820.00 eV # Charge augmentation cutoff

# Ionic Relaxations
EDIFFG = -2E-02 # Stopping criterion for ionic forces
NSW = 100 # Number of steps for ionic relaxation
IBRION = 1 # Ionic relaxation algorithm: Conjugate Gradient (CG)
ISIF = 3 # Relaxation of ions and cell shape
ISYM = 0 # Symmetry: 0 = none, 2 = GGA, 3 = hybrids

# van der Waals Interactions
IVDW = 12 # van der Waals correction with damping

# End of INCAR file
```

Figure 6: Sample INCAR file of VASP.

2. POSCAR

The POSCAR file specifies the atomic positions and cell parameters for the system under study. It defines the initial atomic configuration for the calculation. This file is generated using the VESTA software. It contains the initial lattice parameters in Angstrom. It also gives information about the type and number of atoms. A sample POSCAR file for 2D monolayer of the LaFeO₃ perovskite is shown in Figure 7.

```

2D_LaFeO3
1.0
      7.7213997841      0.0000000000      0.0000000000
      0.0000000000      7.7213997841      0.0000000000
      0.0000000000      0.0000000000      15.0000000000
    La   Fe   O
      4   4   12
Direct
0.925249994      0.606339991      0.567219973
0.425249994      0.606339991      0.567219973
0.925249994      0.106339999      0.567219973
0.425249994      0.106339999      0.567219973
0.174630001      0.345860004      0.725049973
0.674629986      0.345860004      0.725049973
0.174630001      0.845860004      0.725049973
0.674629986      0.845860004      0.725049973
0.174630001      0.595860004      0.725049973
0.424629986      0.345860004      0.725049973
0.175249994      0.356339991      0.567219973
0.674629986      0.595860004      0.725049973
0.924629986      0.345860004      0.725049973
0.675249994      0.356339991      0.567219973
0.174630001      0.095859997      0.725049973
0.424629986      0.845860004      0.725049973
0.175249994      0.856339991      0.567219973
0.674629986      0.095859997      0.725049973
0.924629986      0.845860004      0.725049973
0.675249994      0.856339991      0.567219973

```

Figure 7: Sample POSCAR file of VASP.

3. POTCAR

POTCAR file contains information about the pseudopotentials or projector-augmented-wave (PAW) potentials used to describe the electron-ion interactions in the system. It contains information on pseudo-potentials for all the atoms in the system. The POTCAR file additionally includes details about the atoms, such as their mass (POMASS), number of valence electrons (ZVAL), and the energy of the reference configuration used to generate the pseudopotential. The POTCAR files also contain a default energy cutoff. A snippet of the POTCAR file that contains information about the atoms La, Fe, and O is shown in Figure 8 below.

```

PAW_PBE La 06Sep2000
11.00000000000000
parameters from PSTR are:
SHA256 = b7aad99517e50aeb53363b20a29bb0dfa896544080812fb23322f071df953199 La/POTCAR
COPYR = (c) Copyright 06Sep2000 Georg Kresse
COPYR = This file is part of the software VASP. Any use, copying, and all other rights are regulated by the VASP license agreement.
COPYR = If you do not have a valid VASP license, you may not use, copy or distribute this file.
VRHFIN =La : [core=Kr4d]
LEXCH = PE
EATOM = 865.9763 eV, 63.6475 Ry

TITEL = PAW_PBE La 06Sep2000
LULTRA = F use ultrasoft PP ?
IUNSCR = 1 unscreen: 0-lin 1-nonlin 2-no
RPAOR = 2.300 partial core radius
POMASS = 138.900; ZVAL = 11.000 mass and valenz
RCORE = 2.800 outmost cutoff radius
RWIGS = 2.900; RWIGS = 1.535 wigner-seitz radius (au A)
ENMAX = 219.292; ENMIN = 164.469 eV
RCLOC = 1.601 cutoff for local pot
LCOR = T correct aug charges
LPAW = T paw PP
EAUG = 583.575
DEXC = 0.000
RMAX = 2.853 core radius for proj-oper
RAUG = 1.300 factor for augmentation sphere
RDEP = 2.802 radius for radial grids
RDEPT = 2.156 core radius for aug-charge

Atomic configuration
14 entries
  n  l  j      E      occ.
  1  0  0.50 -38741.0879 2.0000
  2  0  0.50 -6166.6801 2.0000
  2  1  1.50 -5526.1593 6.0000
  3  0  0.50 -1319.0200 2.0000
  3  1  1.50 -1114.5963 6.0000
  3  2  2.50 -821.1793 10.0000

```

Figure 8: Snippet of the POTCAR file of VASP

4. KPOINTS

The KPOINTS file specifies the Bloch vectors (k points) utilized for sampling the Brillouin zone. Achieving convergence in this sampling is crucial for various calculations involving electronic minimization. It determines the accuracy of electronic structure calculations and the resolution of reciprocal lattice points. A sample KPOINTS file is given in Figure 9 where the Monkhorst-Pack has been used. This KPOINTS file is for the 2D monolayer of LaFeO_3 .

```

K-Spacing Value to Generate K-Mesh: 0.040
0
Monkhorst-Pack
  4  4  1
0.0 0.0 0.0

```

Figure 9: Sample KPOINTS file of VASP.

Additionally, VASP generates output files that provide significant information about our system. Some of the significant output files are discussed below:

1. CONTCAR

The CONTCAR file stores the final atomic positions and cell parameters obtained after relaxation or optimization calculations. It serves as a checkpoint file for subsequent calculations. The CONTCAR file holds structural data, including the positions of ions. Its format is compatible with the POSCAR file, making it easy to interchange between them. This file is generated after each ionic step and at the end of a calculation, allowing it to be copied to the POSCAR file for restarting a calculation. A sample CONTCAR file is shown in Figure 10 below which contains the optimized structural parameters of 2D monolayer LaFeO_3 after the structure relaxation step.

```

2D_LaFeO3
1.0000000000000000
| 7.4000259834623678 -0.0001045791975748 0.0071044541961868
-0.0000905410631403 7.3989316590879355 0.0995913422913167
0.0149027528471793 0.2185475350353822 11.4770813148900857
La Fe O
| 4 4 12
Direct
0.9251272460358710 0.6040089538137794 0.5823084477351395
0.4251664653459510 0.6040136672948405 0.5823074963716892
0.9251163779123215 0.1040952006242134 0.5823087920572771
0.4251851105784549 0.1041020748322379 0.5823053574861944
0.1746295505103571 0.3465450376095275 0.7320168733592713
0.6746290526777733 0.3465091507362679 0.7320702999424926
0.1746197170174123 0.8465505620457371 0.7319336063800911
0.6746183829704421 0.8465094640772074 0.7319887234568060
0.1746417990787967 0.5967623786627104 0.7267568123010451
0.4246452861699339 0.3468124316475421 0.7268317769403919
0.1753261924010271 0.3561463201987301 0.5417555011581811
0.6746491451562434 0.5967375611118799 0.7267938435830403
0.9246514113916934 0.3467984958786543 0.7268376211545808
0.6753275556859208 0.3560269743644481 0.5417843435354834
0.1746548599146113 0.0968010244287544 0.7267312212517402
0.4246261333448852 0.8468115210749748 0.7267161303711750
0.1753061849506143 0.8560957666916300 0.5416936520812737
0.6746391721680870 0.0968300002063382 0.7267996622340496
0.9246841551839178 0.8468201464195569 0.7267235176554712
0.6753160455056187 0.8560632462809881 0.5416957809445583

0.00000000E+00 0.00000000E+00 0.00000000E+00

```

Figure 10: Snippet of the CONTCAR file of VASP.

2. CHGCAR

The CHGCAR file stores both the charge density and the occupancies of the PAW one-center functions.

The CHGCAR file comprises of the following blocks:

- Structure in POSCAR format.
- FFT-grid dimensions NGXF, NGYF, NGZF.
- Charge multiplied by FFT-grid volume, with multiple real numbers per line until all NGXF*NGYF*NGZF values of the block are written.
- Augmentation occupancies.

The output file CHGCAR is generally a heavy one, hence a snippet of this file is shown in Figure 11.

Figure 12 represents how this CHGCAR file can be visualized for 2D monolayer LaFeO₃ when imposed on top of the CONTCAR file.

```

2D_LaFeO3
1.0000000000000000
 7.400026   -0.000105    0.007104
-0.000091   7.398932    0.099591
 0.014903   0.218548    11.477081
La   Fe   O
 4   4   12
Direct
0.925127  0.604009  0.582308
0.425166  0.604014  0.582307
0.925116  0.104095  0.582309
0.425185  0.104102  0.582305
0.174630  0.346545  0.732017
0.674629  0.346509  0.732070
0.174620  0.846551  0.731934
0.674618  0.846509  0.731989
0.174642  0.596762  0.726757
0.424645  0.346812  0.726832
0.175326  0.356146  0.541756
0.674649  0.596738  0.726794
0.924651  0.346798  0.726838
0.675328  0.356027  0.541784
0.174655  0.096801  0.726731
0.424626  0.846812  0.726716
0.175306  0.856096  0.541694
0.674639  0.096830  0.726800
0.924684  0.846820  0.726724
0.675316  0.856063  0.541696

80   80   128
0.81995605336E-01  0.84970244922E-01  0.88682728209E-01  0.92443212639E-01  0.96457036360E-01
0.10045140289E+00  0.10455707930E+00  0.10816101769E+00  0.11251276384E+00  0.11560783005E+00
0.11815110318E+00  0.12013498829E+00  0.12208572977E+00  0.12346046674E+00  0.12381503482E+00
0.12329292502E+00  0.12174361468E+00  0.11968716369E+00  0.11755895861E+00  0.11494704810E+00
0.11172212607E+00  0.10734260521E+00  0.10375240363E+00  0.99604246274E-01  0.95640196488E-01
0.91638203761E-01  0.87933876404E-01  0.84283072723E-01  0.81400785039E-01  0.78459137314E-01
0.76217044417E-01  0.75185961721E-01  0.74101048755E-01  0.73149320709E-01  0.72778059308E-01
0.73292957190E-01  0.74363797822E-01  0.75547172235E-01  0.76720503938E-01  0.79173879574E-01

```

Figure 11: Snippet of the CHGCAR file of VASP.

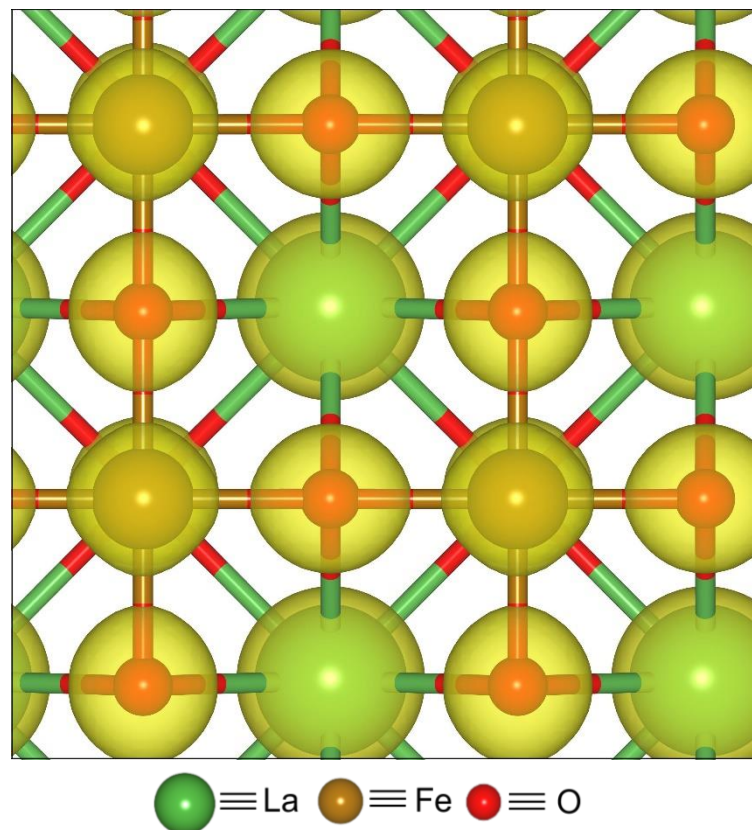


Figure 12: Visualization of the CHGCAR file of VASP.

3. OUTCAR

The OUTCAR file provides comprehensive output from a VASP calculation, which includes:

- Summary of the input parameters used for the calculation.
- Information regarding electronic steps and Kohn Sham-eigenvalues.
- Stress tensors, which describe internal forces within the system.
- Forces acting on individual atoms within the structure.
- Local charges and magnetic moments associated with the atoms.
- Dielectric properties, which describe the response of the material to an external electric field.

2.3 Computational Modelling

To obtain equilibrium geometries, crystal structure, lattice constants, and electronic properties like the electronic band structure, band gap (E_g), and the total density of states (DOS), the First-principles Density Functional Theory (DFT) based calculations were performed in this study using Vienna Ab-Initio Simulation Package (VASP), which is a powerful software based on DFT and is efficiently designed for studying materials with periodic boundary conditions.^{22–24} The computation was done in reciprocal space and plane wave basis sets with an adequate cut-off energy of 450 eV were used. The electron-ion core interactions were characterized by the Projector Augmented Wave (PAW) method.²⁵ The exchange-correlation functional was described by the Perdew-Burke-Ernzerhof exchange (PBE) correlation within the generalized gradient approximation (GGA) method.^{26,27} Spin polarization was incorporated into all the Density Functional Theory (DFT) calculations by using the tag “ISPIN” in the input file INCAR of the VASP code. The 3D bulk LaFeO₃ crystal structure was optimized using the GGA+U method to incorporate the effect of on-site Coulomb interactions using a U_{eff} value of 5.0 eV.²⁸ We have used a $4 \times 4 \times 4$ Monkhorst-pack k-point grid for the 3D bulk LaFeO₃ crystal structure.²⁹ To optimize the orbitals, the RMM-DIIS (Residual minimization method direct inversion in the iterative subspace) algorithm was employed. To explore the ORR mechanism, the (001) plane was cleaved from the 3D bulk LaFeO₃ crystal structure to computationally model a 2D monolayer of LaFeO₃, and the unit cell was increased to a 2×2 supercell, keeping a vacuum thickness of 15 Å in the z-direction for surface isolation to prevent interaction between two neighboring surfaces. This monolayer was then optimized allowing the degrees of freedom (ionic positions, cell volume, and cell shape) to reach equilibrium using the “ISIF” tag in the INCAR file. Here we applied the GGA+U method to reduce the self-interaction error and improve the description of correlation effects. The k-point sampling of Brillouin zone integration was implemented on a grid of $4 \times 4 \times 1$ Monkhorst-pack method for relaxation and for further electronic properties calculation. Both 3D and 2D LaFeO₃ were optimized by reducing the Hellman-Feynman force acting on each ion to less than -0.01

eV Å⁻¹. Total energy convergence was set to 10⁻⁴ eV. Once our system reached equilibrium and the single-point energy calculations were performed, we delved deeper into the electronic properties of both the 3D bulk LaFeO₃ crystal structure and the 2D monolayer of the LaFeO₃ perovskite material. To visualize the band structure, the highly symmetric $\Gamma - R - M - X - T - Z - \Gamma$ and $\Gamma - X - M - \Gamma$ k-vector path in the first Brillouin zone were chosen for 3D bulk LaFeO₃ and 2D monolayer LaFeO₃ respectively. VESTA software was used to visualize all the optimized 2D monolayer structures. To obtain the transition state and the activation barrier for O₂ dissociation on the surface of 2D monolayer LaFeO₃, the climbing-image nudged elastic band (CI-NEB) method implemented in VASP was used.³⁰ The transition state was confirmed by relaxing the structure and performing vibrational frequency calculation of this optimized transition state structure until it reached the convergence threshold of 10⁻⁷ eV in energy and -2 X 10⁻⁴ eVÅ⁻¹ in force. The presence of a single imaginary frequency confirmed the transition state structure.

2.4 Oxygen Reduction Reaction

Oxygen reduction reaction (ORR) has been the subject of extensive research over the last century. This is mainly because ORR is at the heart of energy conversion, particularly in the field of fuel cells and metal-air batteries. The oxygen reduction reaction refers to the reduction half-reaction whereby O₂ is reduced to water. In fuel cells, oxygen from the air is reduced to water at the cathode through the oxygen reduction reaction. Among all the catalysts examined, Pt remains the most effective catalyst for ORR.^{31,32} However, a significant challenge associated with Pt is its classification within the platinum group of metals, which are scarce and thus are expensive for the practical commercialization of fuel cells. Consequently, there has been increased research aimed at discovering alternative electrocatalysts. The reduction of oxygen to water is facilitated through a series of intermediate steps and studying each of these in detail is crucial for a holistic understanding of the ORR process. This reduction process can either follow a direct four-electron pathway where O₂ is directly reduced to H₂O or a slower and indirect two-electron pathway where the reduction takes place via an additional step that includes the formation of H₂O₂.^{33,34} Two-electron pathway in an acidic medium is given as follows:



The four-electron reduction pathway in an acidic medium is expressed as follows:



Based on previous studies, the four-electron reduction pathway is more efficient and is followed by catalysts that exhibit high activity towards ORR.³⁵ Following the framework developed by Norskov et al.,

the overall reduction of O_2 to H_2O through the four-electron reduction pathway shown above can occur through two different mechanisms: the associative reaction mechanism or the dissociative reaction mechanism.³⁶ The ORR process in both of these mechanisms is initiated by the adsorption of O_2 onto the active site on the surface of the material, and after progressing through a continuum of intermediate steps, the adsorbed O_2 gets reduced to ultimately yield water. This first step accounts for the most crucial step for the entire ORR. The associative mechanism follows the process of formation of an OOH^* intermediate by the hydrogenation of adsorbed O_2 , whereas the dissociative mechanism splits the adsorbed O_2 into two atomic O^* which end up getting adsorbed onto two different metal active sites on the surface of the material. The proposed reaction mechanisms of both the associative and the dissociative mechanisms for a general ABO_3 perovskite, following the four-electron reduction pathway have been presented in Figures 13a and Figure 13b respectively.

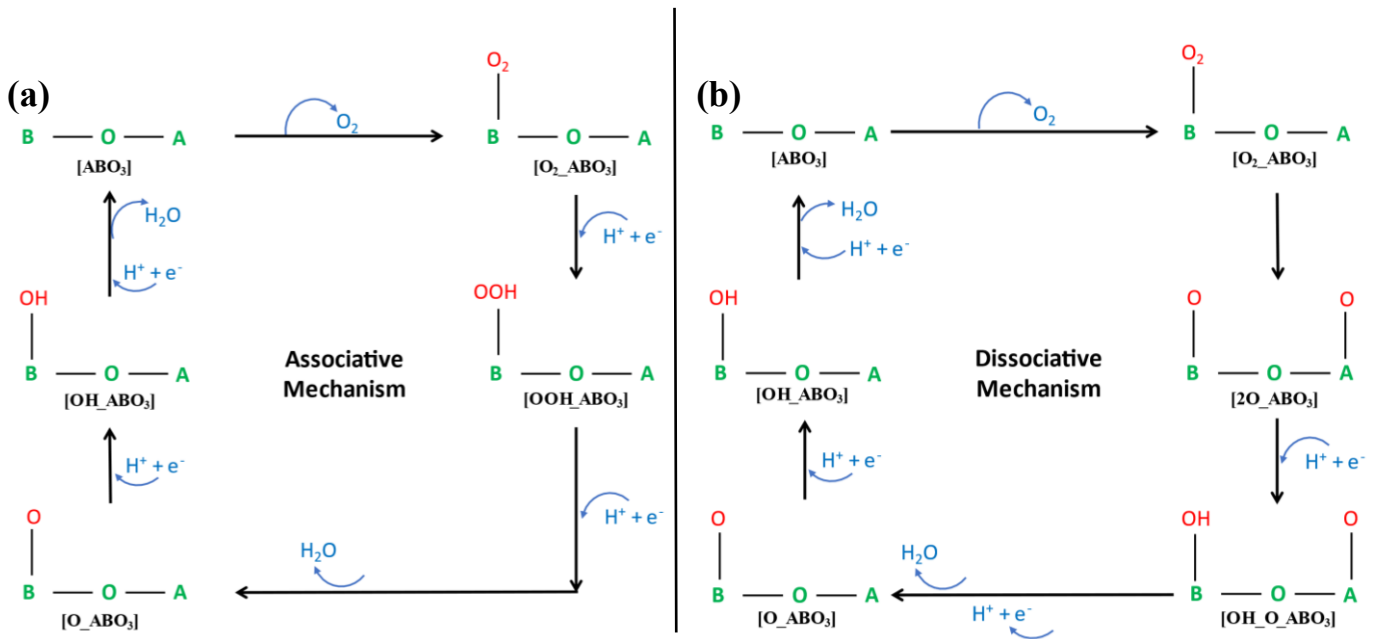
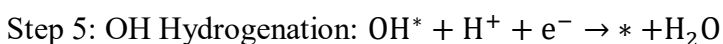
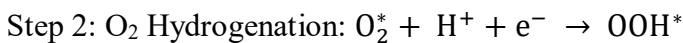
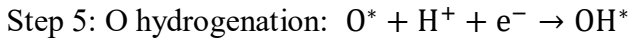
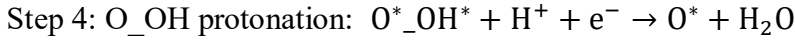
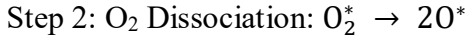


Figure 13: Reaction pathway of (a) Associative mechanism, and (b) Dissociative mechanism of ORR.

The associative mechanism involves the following single-electron intermediate elementary reaction steps in acidic medium:



In the above reaction steps, * indicates the active site on the surface of the catalyst and OOH*, O*, and OH* are the adsorbed intermediate species. The first step in the dissociative mechanism is the same as the associative one, i.e., the adsorption of O₂. The subsequent intermediate steps for the reduction of O₂ in acidic medium are given as follows:



In the above equations the asterisk (*) mark represents the adsorption site. The dissociative pathway involves the cleavage of O-O double bond to form O₂ which gets adsorbed onto two active metal sites. On the cathode, breaking the O-O double bond is rather difficult due to its extremely high bond energy (498 kJ/mol) and this makes the dissociative pathway less probable for most catalysts. In this work, we have computationally explored both the associative and the dissociative mechanisms along with all the reaction intermediates on the surface of 2D monolayer LaFeO₃ perovskite material taking Fe as the active metal site. Based on thermodynamic and energy calculations it was found that the associative mechanism is more favorable for the 2D LaFeO₃ perovskite material. In conclusion, we can infer that the reduction of oxygen basically relies on the O=O bond cleavage and protonation of the ORR intermediates.

2.5 Equations for Energy Calculation and Thermodynamic Analysis

We evaluated the catalytic performance of 2D LaFeO₃ by calculating the adsorption energy (ΔE_{ads}) of the adsorbate on the catalytic surface and the values of change in Gibbs Free energy (ΔG) for each reaction intermediate of the oxygen reduction reaction process using the computational hydrogen electrode (CHE) model as proposed by Norskov et al. and the equations can be formulated as follows:³⁷

$$\Delta E_{ads} = E_{adsorbate+surface} - (E_{surface} + E_{adsorbate}) \quad (55)$$

where, $E_{adsorbate+surface}$, $E_{surface}$ and, $E_{adsorbate}$ are the energies of adsorbed surface, pristine surface, and adsorbate respectively. To determine the change in free energy (ΔG) of all the elementary reaction steps of ORR, the following equation was used:

$$\Delta G = \Delta E + \Delta E_{ZPE} - T\Delta S + \Delta G_{pH} \quad (56)$$

Where ΔE represents the total energy change which is obtained from DFT calculations of the equilibrium structures, ΔE_{ZPE} and ΔS represent the change in zero-point energy and entropy, respectively at room temperature ($T = 298.15\text{K}$). The entropy of gas molecules was taken from the NIST database and the values of ΔE_{ZPE} and $T\Delta S$ were generated from VASPKIT after performing vibrational frequency calculation for each reaction step. ΔG_{pH} is the free energy correction due to H^+ ion concentration and its value is taken as zero in the present work for acidic medium. The free energy of $(\text{H}^+ + \text{e}^-)$ was considered to be that of $\frac{1}{2}(\text{H}_2)$ in the gaseous state which was determined using the SHE. In the present theoretical study, we have taken the 2D monolayer of LaFeO_3 as the standard reference state for calculating the adsorption energies and free energies of all reaction intermediates.

It is important to mention here that negative adsorption energy (ΔE_{ads}) indicates that the reaction is exothermic and that the system is energetically stable. In simpler terms, a negative adsorption energy suggests that the adsorbate is prone to energetically bind to the catalyst surface, indicating a favorable interaction between them.³⁸

Chapter 3

Results and Discussions

3.1 Equilibrium properties of both the 3D bulk and 2D monolayer LaFeO₃

To begin with, the 3D bulk crystal structure of the LaFeO₃ perovskite was optimized, and thereafter its electronic properties, including the electronic band structure, Fermi energy (E_f), electronic band gap (E_g) and the total density of states (DOS) were computed employing the first-principles based density functional theory (DFT) method by using the GGA+U scheme implemented in VASP suite code. The accuracy of GGA functionals is often insufficient for describing strongly correlated electron systems with localized the d orbitals. In such scenarios, an on-site Coulomb interaction with an effective Hubbard U parameter (GGA+U) was incorporated during all the calculations. This method does not distinguish between on-site Coulomb (U) and exchange (J) parameters, as only their difference (U-J) is physically meaningful. Thus, we consider a single parameter $U_{eff} = (U-J)$. Based on previous studies, we have considered $U_{eff} = 5.0$ eV for LaFeO₃ for the d -orbitals of the Fe atom.²⁸ The structure of the 3D bulk LaFeO₃ perovskite is cubic with $Pm\bar{3}m$ space group symmetry which aligns with the previous findings.³⁹ The equilibrium geometry of 3D LaFeO₃ perovskite is presented in Figure 14(a). The optimized unit cell parameters i.e., the lattice constants were found to be $a = b = c = 3.94\text{\AA}$ and $\alpha = \beta = \gamma = 90.0^\circ$ of the 3D LaFeO₃ and these findings are close to the previously reported experimental values.⁴⁰ The equilibrium Fe-O and La-O bond distances of the 3D crystal structure of LaFeO₃ were found to be 1.93\AA , and 2.73\AA , respectively. To gain insights into the electron distribution on the surface of 3D LaFeO₃ and to examine its ORR catalytic activity, the electronic properties of the material were computed and analyzed. At first, the band structure was plotted for both spin-up and spin-down electrons along the highly symmetric k-vector path $\Gamma - R - M - X - T - Z - \Gamma$ with respect to vacuum. A total of sixteen electronic bands were plotted around the Fermi energy level, which consists of eight conduction bands and eight valence bands as depicted in Figure 14b. The solid lines in the band structure plot depict the spin-up electrons and the dotted lines correspond to the spin-down electrons; this convention is followed throughout this work. Our present investigation revealed that the 3D LaFeO₃ has an indirect electronic band gap (E_g) of 0.80 eV, showcasing its semi-metallic properties. Under the same level of theory, the total electron density of states (DOS) was computed, as presented in Figure 14c. The DOS profile is well consistent with the results obtained from the band structure calculations. Negligible electron density is present near the Fermi level as can be seen from the plot of the total DOS of 3D LaFeO₃. This confirms the semi-metallic nature of the 3D LaFeO₃ perovskite material. Table 1 presents a comparison between the results obtained from the current calculation and the previously reported experimental results.

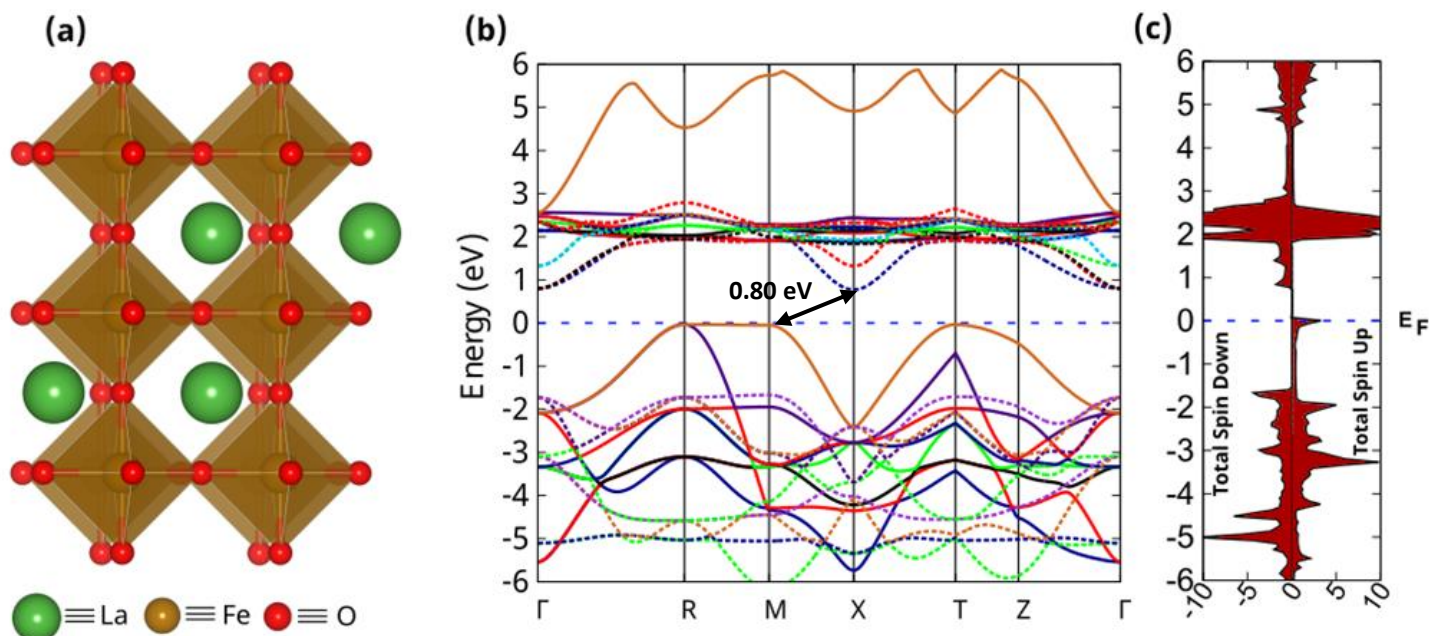


Figure 14: (a) Equilibrium crystal structure, (b) electronic band structure, and (c) total density of states (DOS) of the 3D LaFeO₃ perovskite.

Table 1: Equilibrium lattice constants of the 3D LaFeO₃ crystal structure

System	Lattice constant (a, b, c in Å)	Angle (α, β, γ in degree)	Space group symmetry	Bond distance (Å)	Band gap E_g (eV)	Reference
3D LaFeO ₃	a = b = c = 3.94	$\alpha = \beta = \gamma = 90.0$	$Pm\bar{3}m$	Fe-O: 1.93 La-O: 2.73	0.80	This work
3D LaFeO ₃ (Experimental)	a = b = c = 3.91	$\alpha = \beta = \gamma = 90.0$	$Pm\bar{3}m$	-	-	39,40
2D LaFeO ₃	a = 13.17Å b = 3.08Å	$\alpha = \beta = \gamma = 90.0^\circ$	$P1$	Fe-O: 1.85 La-O: 2.48	0 eV	This work

The present computational investigation based on comprehensive DFT calculations implied that the 3D LaFeO₃ perovskite material has negligible electron density around the Fermi level which is consistent with the band gap ($E_g=0.80$ eV) of 3D bulk LaFeO₃ obtained from the electronic band structure calculations. The minuscule electron density near the Fermi level implies that there is a limited availability of electrons for the conduction process and that the overall transfer of electrons from the valence band to the conduction band will not take place readily. To facilitate faster transfer of electrons to the reactants during the process of oxygen reduction, external energy will be required, and this implies that the 3D bulk LaFeO₃ material will not be efficient in improving ORR activity at the cathode of fuel cells. Upon broadening our research, we cleaved the (001) plane from the bulk crystal structure of LaFeO₃ and computationally modeled a 2D monolayer of the LaFeO₃ perovskite. To mitigate the potential influence of the periodic boundary

conditions on neighboring slabs, a vacuum space of 15\AA was introduced in the z-direction resulting in asymmetry along the z-axis. Consequently, the 2D monolayer of LaFeO_3 displayed $P1$ layer group symmetry. The size of the unit cell of 2D monolayer LaFeO_3 was increased to form a 2×2 supercell. A 2D monolayer was exfoliated out of the bulk crystal structure of LaFeO_3 to increase the specific surface area and surface atomic ratio which thereby led to an increased number of active sites and hence, an increased catalytic activity. The RMM-DIIS algorithm was employed to obtain the equilibrium crystal structure of the 2D monolayer LaFeO_3 perovskite material as presented in Figure 15a and the equilibrium lattice constants were found to be $a = 13.17\text{\AA}$, $b = 3.08\text{\AA}$ and $\alpha = \beta = \gamma = 90^\circ$. The equilibrium bond distances of Fe-O and La-O were found to be 1.85\AA , and 2.48\AA , respectively. The electronic property calculations were carried out and the resulting electronic band structure and total density of states were analyzed. Both the band structure and total DOS were computed along the highly symmetric $\Gamma - X - M - \Gamma$ direction in the first Brillouin zone. The 2D monolayer of LaFeO_3 exhibited a diminished electronic band gap of 0 eV as compared to 3D LaFeO_3 ($E_g = 0.80\text{ eV}$). The total DOS analysis revealed that high electron density is present near the Fermi level, which points towards metallic properties of the 2D monolayer of the LaFeO_3 perovskite. This implies that the drawback in 3D LaFeO_3 , i.e., the absence of electron density near the Fermi level, has now been surpassed in 2D monolayer LaFeO_3 . The density of states near the Fermi level is contributed by both the La-5d and Fe-3d states, with the contribution from La-5d being higher than that of the Fe-3d. This conclusion was corroborated by the analysis of partial charge density within the energy range from -1.5 eV to 0.5 eV relative to the Fermi level as depicted in Figure 16. Table 1 encapsulates all the details of optimized lattice constants, equilibrium bond lengths, band gap and space group symmetries of both the 3D LaFeO_3 perovskite and 2D monolayer LaFeO_3 perovskite materials.

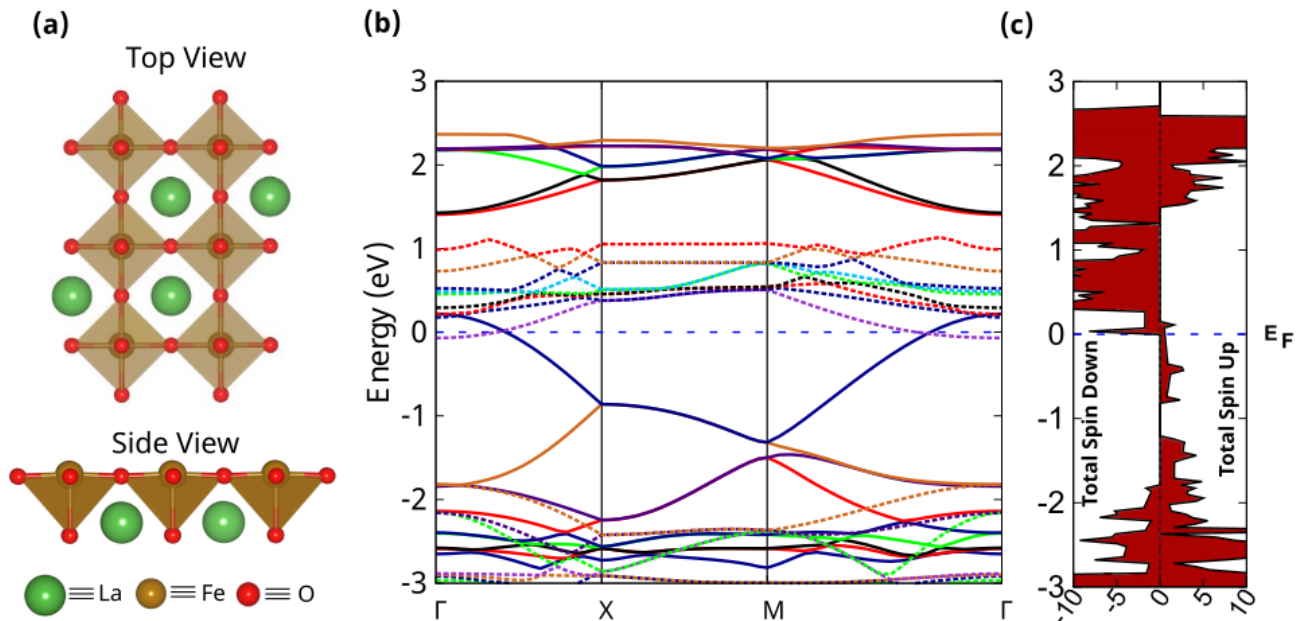


Figure 15: (a) Top and side view of the equilibrium crystal structure of 2D monolayer LaFeO_3 , (b) electronic band structure, and (c) total DOSs of 2D monolayer LaFeO_3

After computing and analyzing the geometrical and electronic properties of both the 3D bulk and 2D monolayer LaFeO_3 , we found that 2D monolayer LaFeO_3 exhibits conductive properties. Consequently, we were keen to know if 2D LaFeO_3 can be useful in improving the sluggish reaction kinetics of ORR at the cathode of fuel cells. To dig deeper into this, we computationally modeled each reaction intermediate of the ORR process and explored both the associative and dissociative reaction pathways by using the periodic slab structure of the 2D monolayer of LaFeO_3 perovskite material in conjunction with the computational hydrogen electrode (CHE) or the standard hydrogen electrode (SHE). Both the associative and the dissociative reaction mechanisms have been explored in an acidic medium and analyzed on the surface of the 2D monolayer of the LaFeO_3 perovskite and the proposed four-electron reduction pathway for LaFeO_3 is presented in Figure 16. All the intermediate structures were computationally modelled and made to reach equilibrium. The relaxed structures of all the reaction intermediates in both the associative and dissociative mechanisms are shown in Figure 17a and Figure 17b, respectively. The adsorbed species are enclosed in a box for clarity. For this study, we have taken the Fe atom as the active site on the (001) surface of the 2D monolayer of LaFeO_3 . Incorporating the impact of a solvent on reaction intermediates during computational modeling poses a significant challenge. This challenge arises due to the strong electric field in the double layer and the dependency of electron free energy in solids on potentials and the free energy of solvated reactants. To address this challenge, a straightforward approach is to correlate the overall trend with gas phase modeling. DFT computations yield highly precise results for gas species, making it easier to calculate electrolytic reactions at the gas-solid interface.

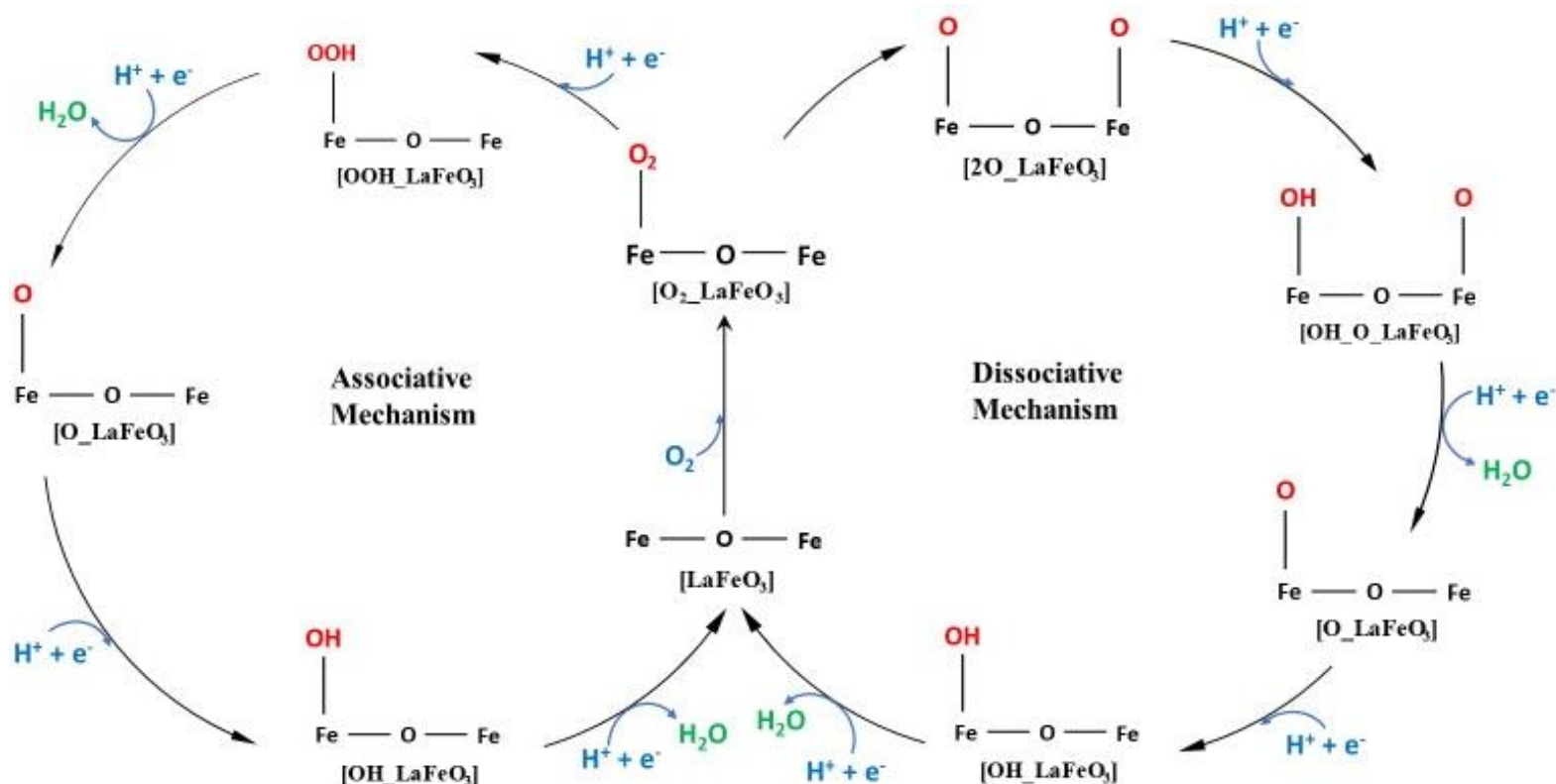


Figure 16: Proposed four-electron associative and dissociative mechanism on the surface of 2D monolayer of the LaFeO_3 perovskite.

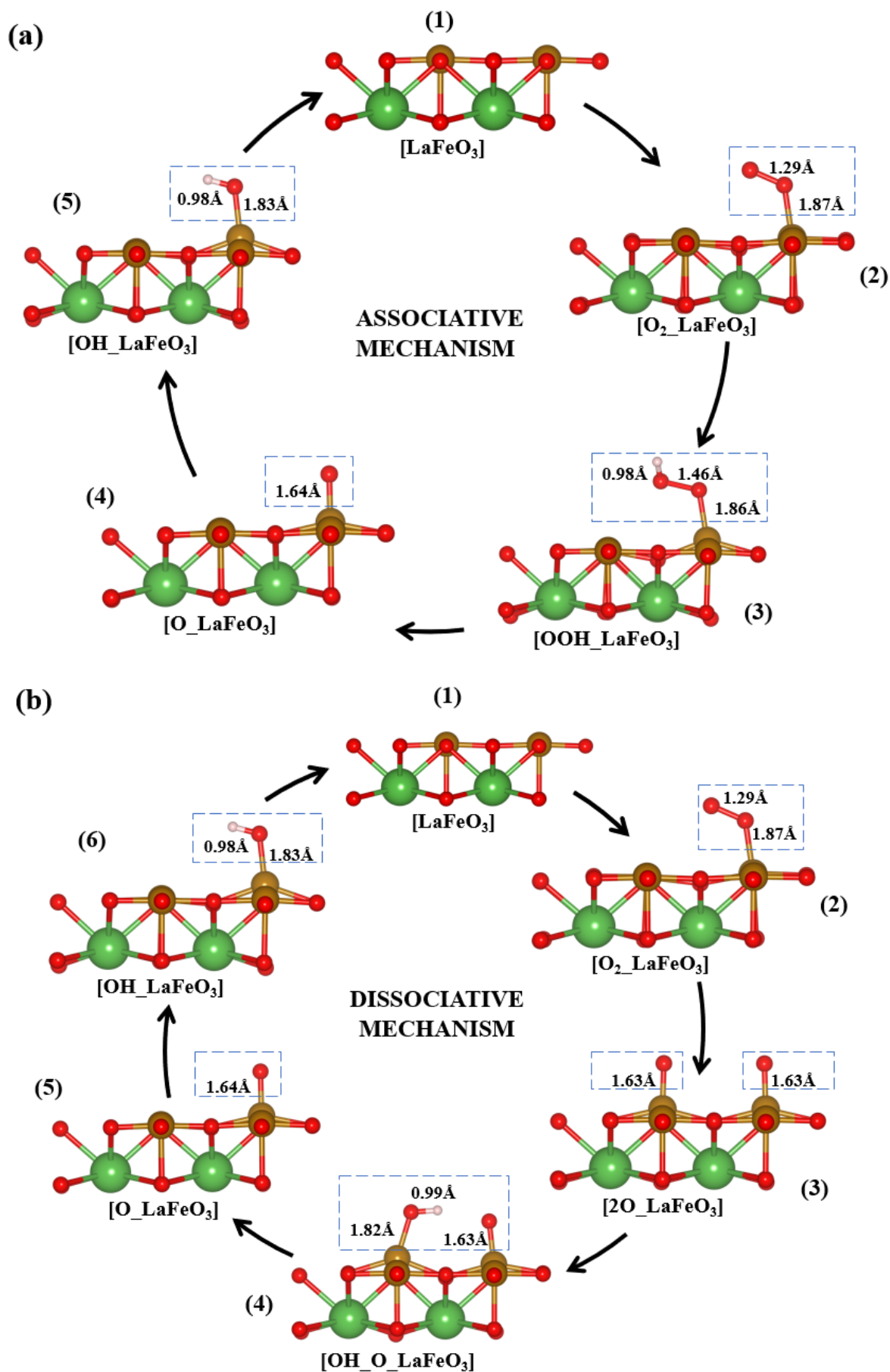


Figure 17: Equilibrium structures of all intermediates of (a) associative mechanism and (b) dissociative mechanism of the oxygen reduction reaction pathway performed on the surface of 2D monolayer LaFeO₃

The mechanism of the reduction of oxygen at the cathode of fuel cells initiates with the critical step of the adsorption of O₂ molecule on the surface of the 2D monolayer of the LaFeO₃ perovskite. The complex so formed after the adsorption of the O₂ molecule is denoted by O₂*_LaFeO₃ where the asterisk mark denotes the active site which is taken as Fe in the present case. According to the Sabatier's principle, efficient catalysis is achieved when the binding strength of the reactants to the catalyst has a moderate value. For a weaker interaction (indicated by a highly positive value of adsorption energy), the population of intermediates decreases significantly, which causes difficulty in starting the reduction process; whereas the case of a stronger binding (highly negative adsorption energy) will lead to the formation of an extremely stable intermediate, which will consequently result in slow dissociation. To begin with, the interaction of the adsorbed O₂ molecule with the active site (Fe) was examined. The adsorption energy for this step was computed to be -0.67 eV which is very close to the value of O₂ adsorption energy on the surface of Pt (111) and Pt (100), which is -0.69 eV and -1.10 eV respectively. From this result, we can infer that the 2D monolayer of the LaFeO₃ perovskite can be a potential electrocatalyst to accelerate the sluggish ORR kinetics.

After the adsorption of O₂ on the surface of the 2D monolayer of LaFeO₃, subsequent steps of oxygen reduction can take place via two pathways: either the associative pathway or the dissociative pathway. In the former, the protonation of the O₂*_LaFeO₃ intermediate takes place to form the OOH*_LaFeO₃ intermediate by the reaction $O_2^*_{LaFeO_3} + H^+ + e^- \rightarrow OOH^*_{LaFeO_3}$. Whilst, in the dissociative mechanism, the adsorbed O₂ molecule dissociates into two atomic O, out of which one remains on the Fe-site and the other one gets adsorbed onto the next active Fe-site. After this step, a series of transfer of protons (H^+) and electrons (e^-) takes place until finally oxygen gets reduced to water. In the present theoretical work, we have studied both the associative and the dissociative reaction mechanisms on the surface of 2D monolayer LaFeO₃ along with all the reaction intermediates. We have computed the values change in Gibbs free energy (ΔG) for all intermediate steps by incorporating the zero-point energy and change of entropy correction using the vibrational frequency calculations in VASP. In the upcoming sections, we have discussed in detail the electronic and structural properties of all the intermediates along with their ΔG values concerning both associative and dissociative reaction mechanisms.

3.2 Associative Mechanism of ORR

Post performing the electronic property calculations, we concluded that 2D monolayer LaFeO₃ exhibits metallic properties. Therefore, we were curious about the ORR activity of this monolayer of the LaFeO₃ perovskite. At the outset, we explored the associative reaction mechanism on the surface of 2D monolayer LaFeO₃. Here we explain all the reaction intermediate steps that are involved in the associative mechanism of the reduction of oxygen.

Step 1: Adsorption of O₂

The reduction of oxygen initiates with the adsorption of O₂ molecule onto the active site of the 2D monolayer slab of LaFeO₃. This step was computationally modelled by attaching an O atom to the Fe atom at a distance of 1.64 Å which is close to the actual value of the Fe-O bond length. Another O atom was attached to this preexisting O atom at a distance of 1.35 Å. This structure was then allowed to reach equilibrium by allowing the positions, cell shape, and cell volume to relax. The complex so formed was denoted by O₂*_LaFeO₃ and the resulting equilibrium structure is shown in Figure 18a. After the structure relaxation calculation, it was found that the equilibrium bond lengths of Fe-O and O-O were 1.87 Å and 1.29 Å respectively. The electronic properties (electronic band structure and total DOS) for the O₂*_LaFeO₃ intermediate were computed as shown in Figure 18b and Figure 18c, respectively. A total number of sixteen bands were plotted around the Fermi level along the highly symmetric $\Gamma - X - M - \Gamma$ k-vector direction which is kept consistent with the k-vector direction used for calculating the electronic band structure for 2D monolayer LaFeO₃. The band gap for the O₂*_LaFeO₃ ORR intermediate was found to be 0.00 eV and the Fermi energy (E_f) was found to be -0.96 eV which is normalized to the zero level of band energy as shown in the band structure plot in Figure 18b. From the band structure calculations, we observe that some bands overlap around the Fermi level which depicts the conducting nature of O₂*_LaFeO₃. To validate this conducting behaviour, the total DOS calculations were carried out along the same k-vector path as shown in Figure 18c. From the DOS profile it is evident that adequate electron density is present around the Fermi level which confirms the metallic characteristics of this O₂*_LaFeO₃ complex. The change in Gibbs free energy (ΔG) for the reaction O₂ + * \rightarrow O₂* was computed to be -0.35 eV. The negative value of ΔG suggests that the adsorption of O₂ on the surface of 2D monolayer LaFeO₃ is exothermic, thermodynamically stable, and kinematically attainable to facilitate O₂ reduction.

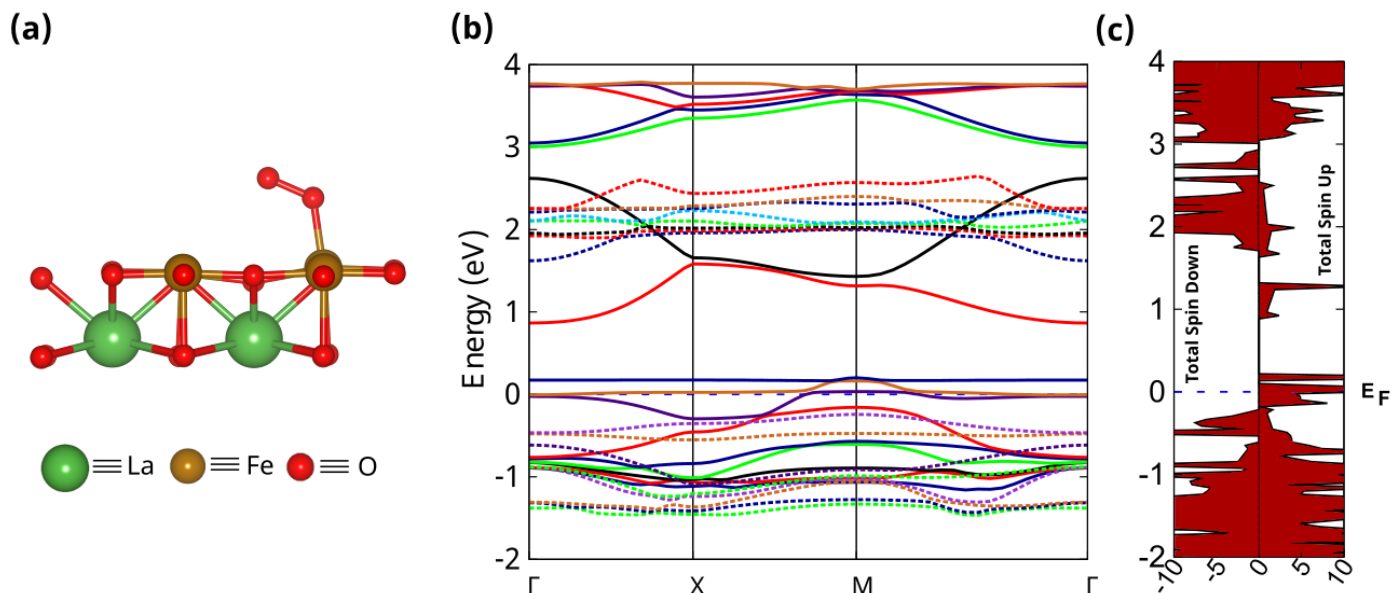


Figure 18: (a) Equilibrium structure, (b) band structure, and (c) total DOS of O_2^* _LaFeO₃

Step 2: Hydrogenation of O₂

The subsequent step in the process of oxygen reduction in the four-electron associative reaction mechanism is the protonation of the activated adsorbed O₂ molecule at the Fe-site of 2D monolayer of LaFeO₃. We computationally modelled this ORR intermediate by placing one H-atom near the outer O atom of O₂*_LaFeO₃. The complex so formed was denoted by OOH*_LaFeO₃. This resulting structure was then relaxed and the equilibrium O-H bond length was found to be 0.98Å which is equal to the standard O-H bond length. In this case, the H⁺ ion that comes from the anode side via the proton exchange membrane and the electron that comes through the external circuit, reacts with the oxygen molecule adsorbed on the Fe-site and leads to the formation of the OOH* intermediate. The equilibrium structure of this complex is shown in Figure 19a. Thereafter, the band structure and density of states calculations were performed for OOH*_LaFeO₃ as shown in Figure 19b and Figure 19c respectively. The Fermi energy (E_F) was found to be -0.65 eV and the electronic band gap was calculated to be 0.00 eV. From the plot of the electronic band structure, we can see that there is a high density of bands near the Fermi level and that the minima of the valence band and the maxima of the conduction band for OOH*_LaFeO₃ are present at the Γ -, and M-points respectively. Using the same level of theory, total DOS was plotted as shown in Figure 19c. The profile of DOSs is well consistent with the electronic band structure calculation and points towards the metallic characteristic of the OOH* intermediate. The value of ΔG was calculated for $O_2^* + H^+ + e^- \rightarrow OOH^*$ reaction and it was found to be -1.08 eV. This negative value of ΔG suggests that the protonation of the adsorbed oxygen molecule on the surface of the 2D monolayer LaFeO₃ to form the OOH* intermediate is spontaneous and thermodynamically favourable. Hence, this reaction continues to the subsequent steps of ORR.

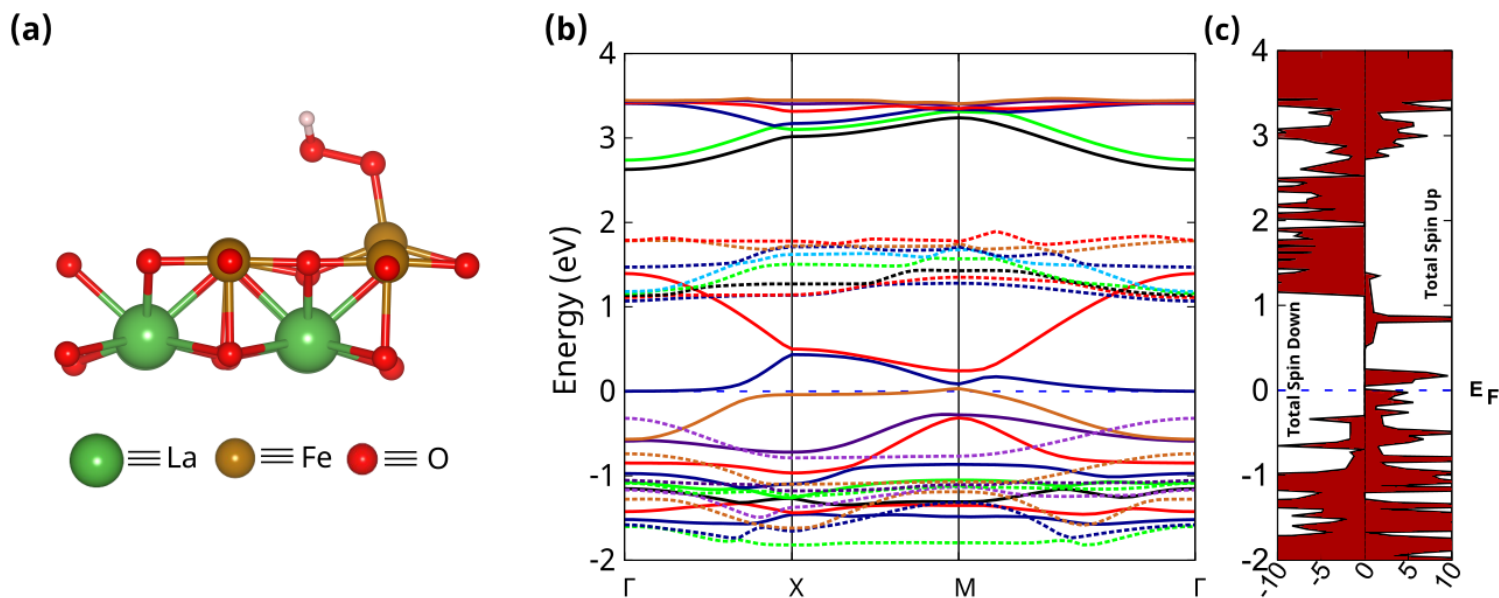


Figure 19: (a) Equilibrium structure, (b) band structure, and (c) total DOS of $\text{OOH}^*_{\text{LaFeO}_3}$

Step 3: Reduction of OOH^* into O^*

The subsequent step of the four-electron associative mechanism of the oxygen reduction reaction is the hydrogenation of the OOH^* intermediate which leads to the formation of the $\text{O}^*_{\text{LaFeO}_3}$ complex. In this step, the proton and electron that reach the cathode side of the fuel cell through the proton exchange membrane and the external circuit respectively, react with the OOH^* species that is adsorbed on the Fe-site and forms the $\text{O}^*_{\text{LaFeO}_3}$ complex. A water molecule is also removed from the surface of 2D monolayer LaFeO_3 amidst this process. This intermediate was computationally modelled by attaching an O atom onto the Fe atom keeping a bond length of 1.66 Å. Upon structure relaxation, the equilibrium Fe-O bond length was found to be 1.64 Å. The equilibrium structure of the $\text{O}^*_{\text{LaFeO}_3}$ reaction intermediate is shown in Figure 20a. To dig deeper into the electronic properties of this intermediate, the band structure and total density of states was plotted as shown in Figure 20b and Figure 20c. The band structure plot for the $\text{O}^*_{\text{LaFeO}_3}$ reaction intermediate shows overlapping of bands at and around the Fermi level which points towards its metallic properties. The band gap (E_g) for the $\text{O}^*_{\text{LaFeO}_3}$ ORR intermediate was determined to be 0.00 eV. To confirm this metallic behaviour, the total DOS was also computed as shown in Figure 20c using the same level of theory and the DOS profile aligns with the value of band gap obtained from the band structure calculations. Electron density is observed near the Fermi level which indicates that enough charge carriers are available for the conduction process. The value of E_f was computed to be -0.76 eV which is normalized to the zero level of the band energy. From these electronic calculations we can infer that both band structure calculations and DOSs profile complement each other. The value of ΔG for this step of hydrogenation of the OOH^* intermediate was calculated to be -0.58 eV. This small and negative

value of the change in Gibbs free energy reveals that the reaction is exothermic, thermodynamically stable, and energetically favourable for the ORR mechanism.

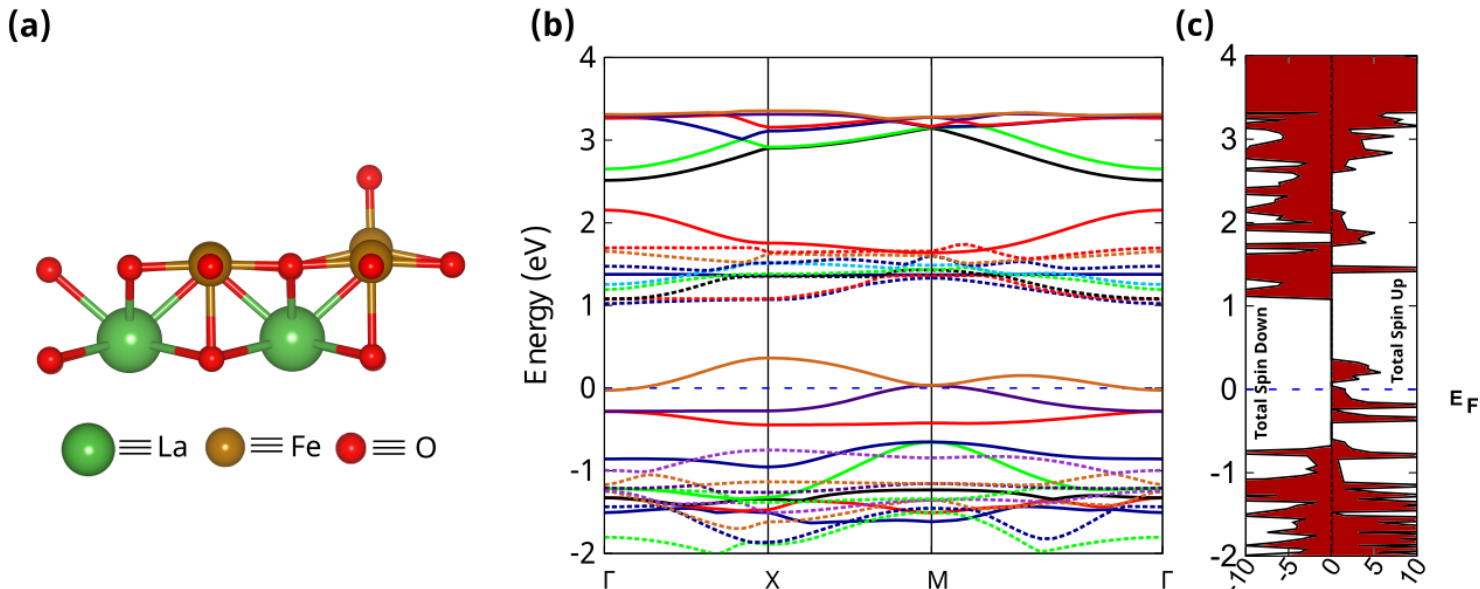


Figure 20: (a) Equilibrium structure, (b) band structure, and (c) total DOS of O*_{LaFeO₃}

Step 4: Protonation of O* to form OH*

The step of hydrogenation of OOH* is followed by the protonation of the O* intermediate to form the complex OH*_{LaFeO₃}. The proton (H⁺) that comes to the cathode (ORR side) through the proton exchange membrane, and the electron (e⁻) that comes via the external circuit from the anode to the cathode side, react with the O-atom which is bonded to the Fe-atom and this leads to the generation of the OH* intermediate. To computationally model this reaction intermediate, we attached an oxygen atom to the iron atom keeping a bond length of 1.66 Å and a hydrogen atom was then attached to this oxygen atom at a distance of 1.07 Å. This OH*_{LaFeO₃} complex was then made to reach equilibrium and the bond lengths of Fe-O and O-H of the resulting equilibrium structure were found to be 1.83 Å and 0.98 Å, respectively. The equilibrium structure of the OH*_{LaFeO₃} complex so formed is given in Figure 21a. To delve into the electronic properties of this complex, band structure and total DOS calculations were performed as shown in Figure 21b, and Figure 21c respectively. The Fermi energy and the band gap were found to be -0.82 eV and 0.01 eV respectively. The band gap of this step is slightly higher than the previous steps of ORR. The valence band minima and the conduction band maxima are found to be located at the M- point as can be seen from the band structure plot. To confirm the results obtained from the band structure calculations, we performed the total density of states calculation of the OH*_{LaFeO₃} intermediate along the highly symmetric $\Gamma - X - M - \Gamma$ k-vector direction. The small band gap of 0.01 eV is evident from the DOS profile. Hence, the band structure and DOS plots agree well with each other. The value of ΔG for this step was calculated to be -1.12 eV. This negative value of change in Gibbs free energy exhibits that this step is exothermic, and hence, this process is thermodynamically and energetically favourable for the reduction of O₂.

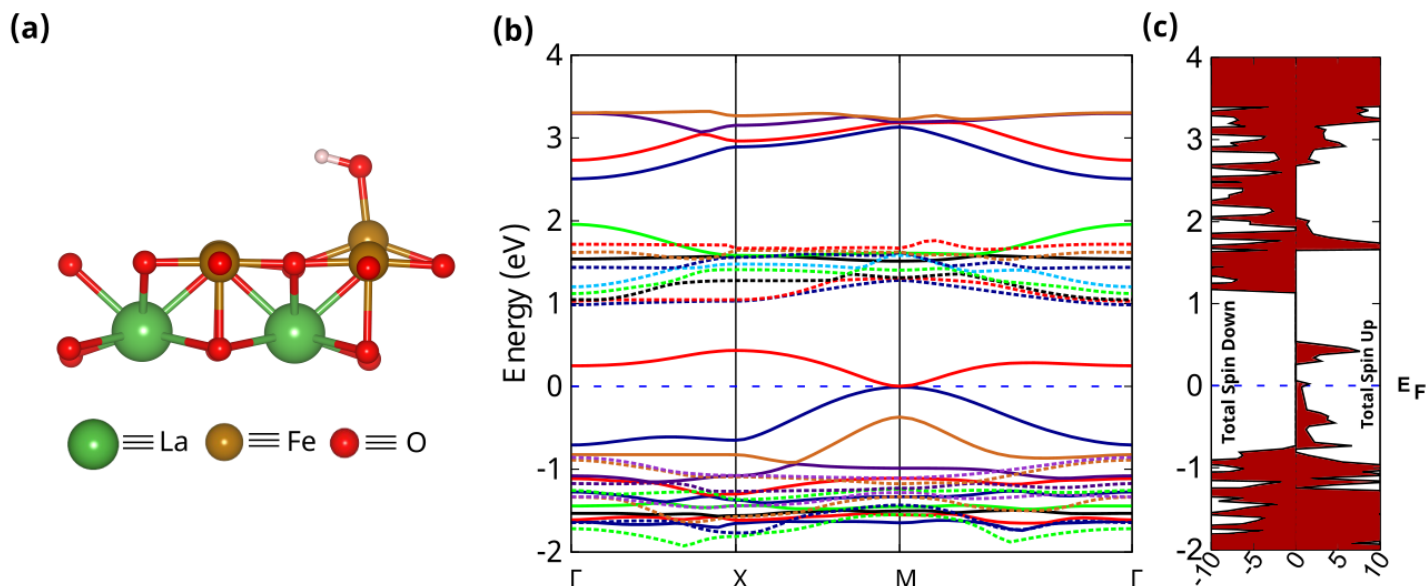


Figure 21: (a) Equilibrium structure, (b) band structure, and (c) total DOS of OH*__{LaFeO₃}

Step 5: Protonation of OH*__{LaFeO₃}

This step marks the final stage of the reduction of oxygen. This last step of the four-electron associative mechanism involves the hydrogenation of the OH* intermediate. The H⁺ and e⁻ that come from the anode side to the cathode side, react with the OH* species adsorbed on the surface of 2D monolayer LaFeO₃ and lead to the formation of a second water molecule of this four-electron associative mechanism. As a result, this water molecule is removed from the surface of the 2D monolayer LaFeO₃ and this marks the reduction of the oxygen molecule completing the transfer of four electrons in total. The value of ΔG for this step was calculated to be -1.72 eV and this points towards the exothermic nature of this step. Hence, this process is thermodynamically and energetically favourable for the ORR process. The value of the change in Gibbs free energy and their relative values for all the reaction steps in the associative mechanism of oxygen reduction on the surface of 2D monolayer LaFeO₃ are listed in Table 2. The 2D monolayer LaFeO₃ structure has been taken as the reference geometry to calculate the relative free energies.

Table 2: Change in Gibbs Free Energy (eV) and the Relative Free Energy (eV) of each reaction step during the reduction of oxygen through the Associative Mechanism.

Various reaction steps involved in the Associative Mechanism	ΔG (eV)	Relative Free Energy (eV)
$\text{LaFeO}_3 + \text{O}_2 \rightarrow \text{O}_2^*_{\text{LaFeO}_3}$	-0.35	-0.35
$\text{O}_2^*_{\text{LaFeO}_3} + \text{H}^+ + \text{e}^- \rightarrow \text{OOH}^*_{\text{LaFeO}_3}$	-1.08	-1.43
$\text{OOH}^*_{\text{LaFeO}_3} + \text{H}^+ + \text{e}^- \rightarrow \text{O}^*_{\text{LaFeO}_3} + \text{H}_2\text{O}$	-0.58	-2.01
$\text{O}^*_{\text{LaFeO}_3} + \text{H}^+ + \text{e}^- \rightarrow \text{OH}^*_{\text{LaFeO}_3}$	-1.12	-3.13
$\text{OH}^*_{\text{LaFeO}_3} + \text{H}^+ + \text{e}^- \rightarrow \text{LaFeO}_3 + \text{H}_2\text{O}$	-1.72	-4.85

3.3 Dissociative Mechanism of ORR

In this theoretical study, we also studied and analysed the four-electron dissociative mechanism of the reduction of oxygen on the surface of the 2D monolayer of the LaFeO₃ perovskite material. The complete dissociative mechanism with each intermediate step is shown in Figure 13b. The first step of the dissociative mechanism is the same as that of the associative mechanism which is the adsorption of O₂ molecule onto the active Fe-site on the surface of the 2D monolayer of the LaFeO₃ perovskite. The subsequent two steps differ from the steps in the four-electron associative pathway, which are the dissociation of O₂^{*}, and the hydrogenation of 2O^{*}. All other steps following this are the same as the associative mechanism. The two steps of the dissociative mechanism that are different from the associative mechanism are explained below.

Dissociation of O₂^{*} into 2O^{*}

After the adsorption of the O₂ molecule on the surface of the 2D monolayer of the LaFeO₃ perovskite material, this oxygen molecule dissociates into two oxygen atoms, out of which one of the oxygen atoms stays at the Fe-site, and the other oxygen atom gets adsorbed onto the next active Fe-site. This leads to the formation of the 2O^{*}_LaFeO₃ complex. To computationally model this reaction intermediate, we attached one oxygen atom each to two nearby iron atoms, setting the Fe-O bond length to 1.66Å for both the oxygen atoms. The resulting 2O^{*}_LaFeO₃ structure was then allowed to reach equilibrium by allowing the relaxation of the atomic positions, cell shape, and cell volume. After the relaxation step, the equilibrium Fe-O bond length was found to be 1.63Å. The resulting equilibrium structure is depicted in Figure 22a. To understand the electronic behaviour of this intermediate, we computed and analysed the electronic band structure and the total density of states using the same level of theory as in the preceding steps. The band structure and the total DOS were plotted along the highly symmetric $\Gamma - X - M - \Gamma$ k-vector direction in the first Brillouin zone. A total of sixteen bands around the Fermi level were plotted for both spin-up and spin-down electrons as shown in Figure 22b. From the plot of the electronic band structure, we can see bands crossing the Fermi level which point towards the metallic behaviour of the 2O^{*}_LaFeO₃ reaction intermediate. The band gap and the Fermi energy were computed to be 0.00 eV and -1.34 eV, respectively. To validate the findings derived from the band structure calculations, the total DOS calculations were also performed. It is evident from the DOSs profile shown in Figure 22c that sufficient electron density is present near the Fermi level to facilitate charge transfer from the valence band to the conduction band. The results of the electronic property calculations reveal the conducting behaviour of the 2O^{*}_LaFeO₃ intermediate complex. The value of ΔG for this reaction step was calculated to be 1.58 eV. This positive value of the change in Gibbs free energy reveals that the process of dissociation of O₂^{*} into 2O^{*} is endothermic and is not a spontaneous one. Thus, after the first step of the adsorption of O₂^{*}, the associative

pathway will be favoured more than the dissociative pathway because of the spontaneity of the formation of OOH* intermediate rather than the 2O* intermediate.

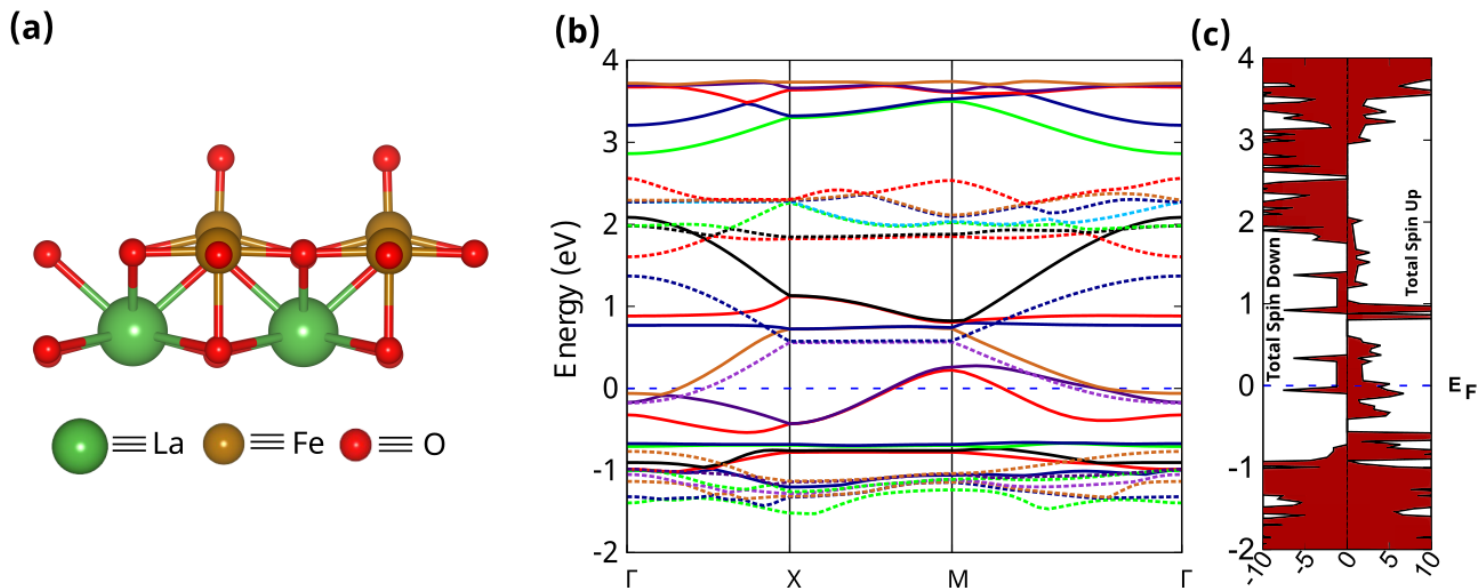


Figure 22: (a) Equilibrium structure, (b) band structure, and (c) total DOS of 2O*₂-LaFeO₃

The transition state calculation was performed for the dissociation of O₂* into 2O* using the Climbing-Image Nudged Elastic Band (CI-NEB) method in VASP, and the activation energy (E_a) was computed. Here, E_a is defined as the energy difference between the transition state (TS) and the initial state (O₂*₂-LaFeO₃). We determined the minimum energy path (MEP) and located the transition state. For the CI-NEB calculations, we started from the lowest-energy adsorption configuration of the reactant which is O₂*₂-LaFeO₃, and ended at the lowest-energy adsorption configuration of the product which is 2O*₂-LaFeO₃. Thereafter, we identified the transition state as the highest-energy configuration in a linear transition path from the initial state to the final state. This TS was confirmed by performing a vibrational frequency analysis on the equilibrium TS structure. During the frequency calculation, the 2D monolayer of the LaFeO₃ material was frozen and only the adsorbed O₂ molecule on the surface was allowed to vibrate. The results of this vibrational frequency analysis showed a single imaginary frequency of -264.48 cm⁻¹ along with some negligible imaginary frequencies which can appear due to various other factors. The presence of one soft mode confirms that the TS structure found is in fact the highest point of the MEP for the dissociation of O₂* into 2O*. The plot of the relative free energy for the TS found for the dissociation of O₂ molecule on the surface of 2D monolayer LaFeO₃ is depicted in Figure 23. The free energy for the initial state (O₂*₂-LaFeO₃), TS, and the final state (2O*₂-LaFeO₃) have been plotted by taking the initial state as the reference geometry. The value of the energy barrier was computed to be 1.8 eV which is very high as compared to the dissociation barrier of O₂ on Pt (111) (0.48 eV). From these findings, we conclude that the reduction of oxygen on the surface of the 2D monolayer of LaFeO₃ through the dissociative mechanism is not favourable.

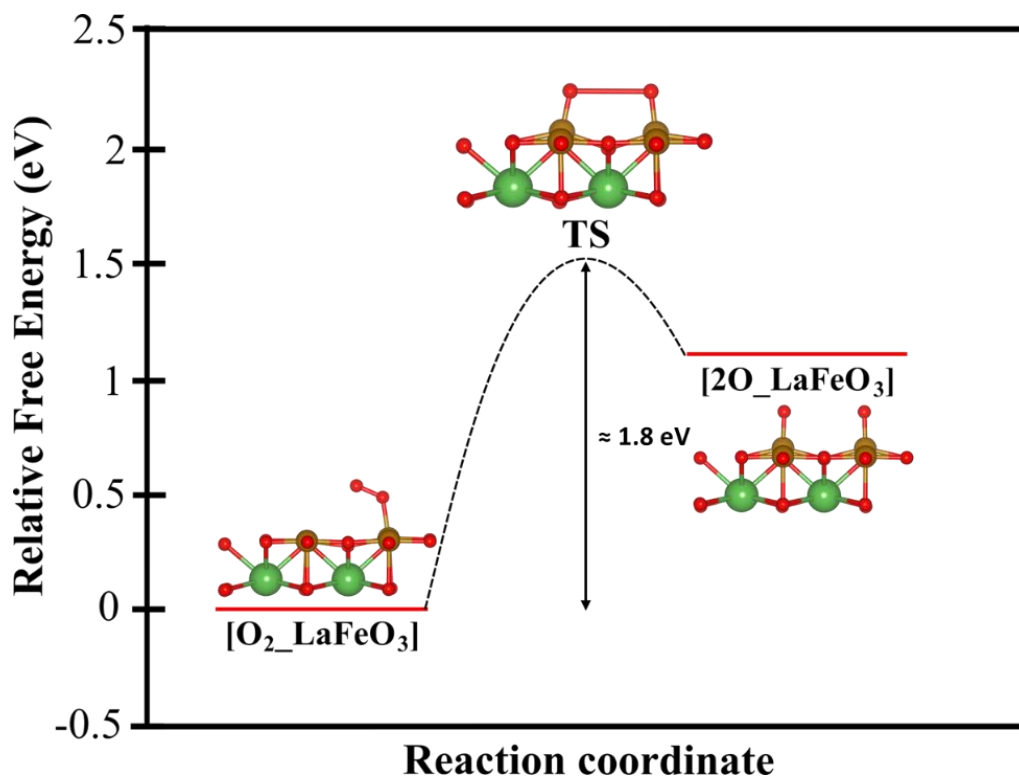


Figure 23: O₂ dissociation of LaFeO₃ monolayer.

Protonation of 2O* to form O*_OH*

After the step of dissociation of O₂, the 2O* species reacts with H⁺ and e⁻ coming from the anode side of fuel cell and the formation of O*_OH*_LaFeO₃ intermediate takes place. To computationally model this intermediate, a hydrogen atom was attached to one of the oxygen atoms of the 2O*_LaFeO₃ intermediate at a distance of 1.07Å. The O*_OH*_LaFeO₃ structure was then made to reach equilibrium and the structure obtained from the structure relaxation step is shown in Figure 24a. The equilibrium bond lengths of Fe-O and O-H were found to be 1.82Å and 0.99Å respectively. The electronic property calculations were also performed using the same DFT methods as in the previous reaction steps. The electronic band structure was plotted along the highly symmetric $\Gamma - X - M - \Gamma$ k-vector direction in the first Brillouin zone which is consistent with the previous band calculations. Total density of states was also calculated and plotted along the same k-vector direction. From the band structure plot of the O*_OH*_LaFeO₃ reaction intermediate of ORR, we calculated that the band gap for this complex is 0.00 eV which is also evident from the crossing of bands on the Fermi level as shown in Figure 24b. To validate the results obtained from the band structure calculations, total DOS was plotted. The DOSs profile shown in Figure 24c aligns with the findings from the band structure calculations which is evident from the high electron density around the Fermi level. Thus, from these results we can infer that the O*_OH*_LaFeO₃ reaction intermediate

exhibits metallic properties. The value of ΔG for this step was found to be -3.25 eV which depicts that this step is exothermic, and thermodynamically and kinetically favourable.

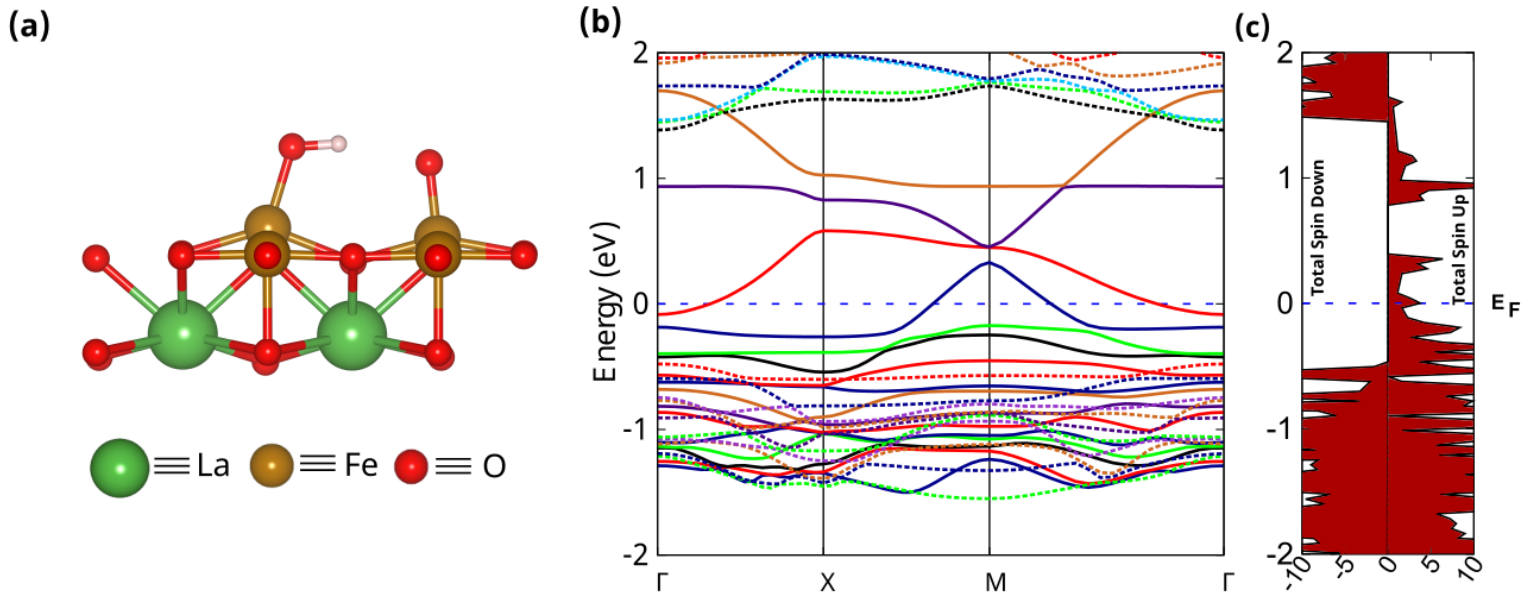


Figure 24: (a) Equilibrium structure, (b) band structure, and (c) total DOS of O* _OH* _LaFeO₃

The change in Gibbs free energy and the relative free energy for all the reaction intermediates of the dissociative mechanism of ORR have been listed in Table 3. The geometrical data of all the equilibrium intermediate geometries have been summarized in Table 4.

Table 3: Change in Gibbs Free Energy (eV) and the Relative Free Energy (eV) of each reaction step during the reduction of oxygen through the Dissociative Mechanism on the surface of the 2D monolayer LaFeO₃ material.

Various reaction steps involved in the Dissociative Mechanism	ΔG (eV)	Relative Free Energy (eV)
$\text{LaFeO}_3 + \text{O}_2 \rightarrow \text{O}_2^* \text{ _LaFeO}_3$	-0.35	-0.35
$\text{O}_2^* \text{ _LaFeO}_3 \rightarrow 2\text{O}^* \text{ _LaFeO}_3$	1.58	1.23
$2\text{O}^* \text{ _LaFeO}_3 + \text{H}^+ + \text{e}^- \rightarrow \text{O}^* \text{ _OH}^* \text{ _LaFeO}_3$	-3.25	-2.02
$\text{O}^* \text{ _OH}^* \text{ _LaFeO}_3 + \text{H}^+ + \text{e}^- \rightarrow \text{O}^* \text{ _LaFeO}_3 + \text{H}_2\text{O}$	0.01	-2.01
$\text{O}^* \text{ _LaFeO}_3 + \text{H}^+ + \text{e}^- \rightarrow \text{OH}^* \text{ _LaFeO}_3$	-1.12	-3.13
$\text{OH}^* \text{ _LaFeO}_3 + \text{H}^+ + \text{e}^- \rightarrow \text{LaFeO}_3 + \text{H}_2\text{O}$	-1.72	-4.85

Table 4: Geometrical data of the equilibrium structures of all the reaction intermediates involved in the Associative and the Dissociative Mechanisms on the surface of 2D monolayer of the LaFeO₃ perovskite material.

Reaction Steps	Lattice Parameters (Å)	Interfacial angles (deg)	Layer group and Symmetry	Electronic Band Gap (eV)	Average bond length (Å)			
					Fe-O	La-O	O-O	O-H
2D LaFeO ₃	a = b = 7.40	$\alpha = \beta = \gamma = 90^\circ$	<i>PI</i>	0.02	1.85	2.48	-	-
O2*_LaFeO ₃	a = b = 7.40	$\alpha = \beta = \gamma = 90^\circ$	<i>PI</i>	0.00	1.87	2.49	1.29	-
2O*_LaFeO ₃	a = b = 7.40	$\alpha = \beta = \gamma = 90^\circ$	<i>PI</i>	0.01	1.63	2.47	-	-
OOH*_LaFeO ₃	a = b = 7.40	$\alpha = \beta = \gamma = 90^\circ$	<i>PI</i>	0.01	1.87	2.53	1.46	0.98
O*_OH*_LaFeO ₃	a = b = 7.40	$\alpha = \beta = \gamma = 90^\circ$	<i>PI</i>	0.01	1.82	2.49	-	0.99
O*_LaFeO ₃	a = b = 7.40	$\alpha = \beta = \gamma = 90^\circ$	<i>PI</i>	0.00	1.64	2.50	-	-
OH*_LaFeO ₃	a = b = 7.40	$\alpha = \beta = \gamma = 90^\circ$	<i>PI</i>	0.01	1.83	2.53	-	0.98

To summarize our results of the present study of the catalytic activity of the LaFeO₃ perovskite material to accelerate the sluggish kinetics of ORR at the cathode of fuel cells, we plotted and analysed the potential energy curve for both associative and dissociative reaction mechanisms as shown in Figure 25 and Figure 26 respectively. The Relative Free Energy was plotted in these potential energy curves in which the 2D monolayer of LaFeO₃ was taken as the reference geometry and the free energy for all other intermediates were plotted relative to this geometry. Under standard conditions (298.15 K temperature and 1 atm pressure), the total ΔG for the complete reaction $O_2 + 2H_2 \rightarrow 2H_2O$ is expected to be -4.92 eV. According to our Gibbs energy analysis, the total ΔG was determined to be -4.85 eV for both the dissociative and associative mechanisms. This ΔG value obtained from our theoretical analysis agrees well with the experimental value. From the potential energy surface (PES) of the associative mechanism we can see that all the steps are downhill which depicts that all the steps of the associative mechanism on the surface of 2D monolayer LaFeO₃ are thermodynamically feasible. Whereas, if we look at the free energy landscape of the dissociative mechanism, we can see that the 2O* step is breaking the downhill trend by a large relative free energy value. The O* step also shows the same break in the downhill trend but by a minor uphill value of relative free energy. These trends depicted in the free energy landscape of the dissociative mechanism points to the fact that the dissociative mechanism is not favourable and that the reduction of oxygen on the surface of 2D monolayer of the LaFeO₃ perovskite material will rather take up the associative pathway than the unstable dissociative pathway. Therefore, the four-electron associative reaction mechanism is the most favourable one for the reduction of oxygen on the surface of 2D monolayer LaFeO₃.

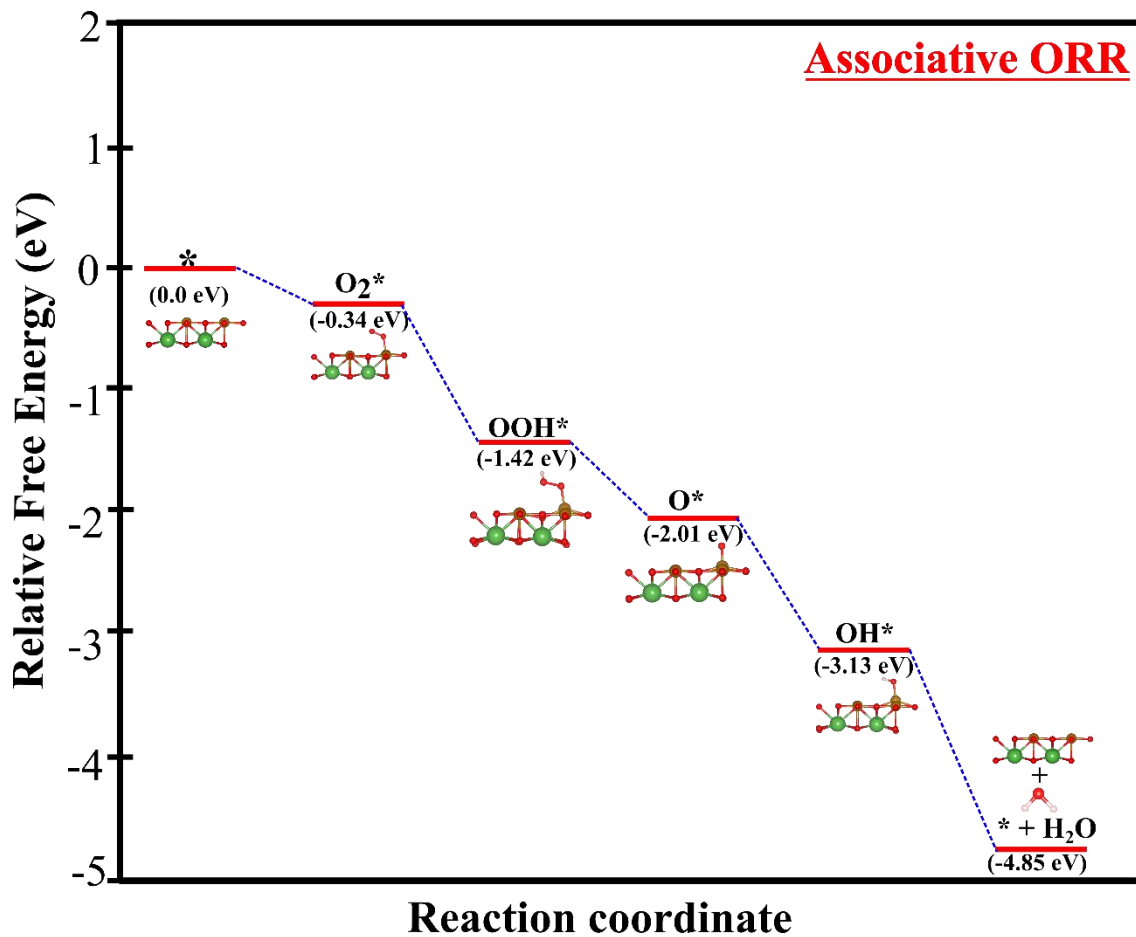


Figure 25: Potential Energy Surface (PES) of the Associative ORR mechanism

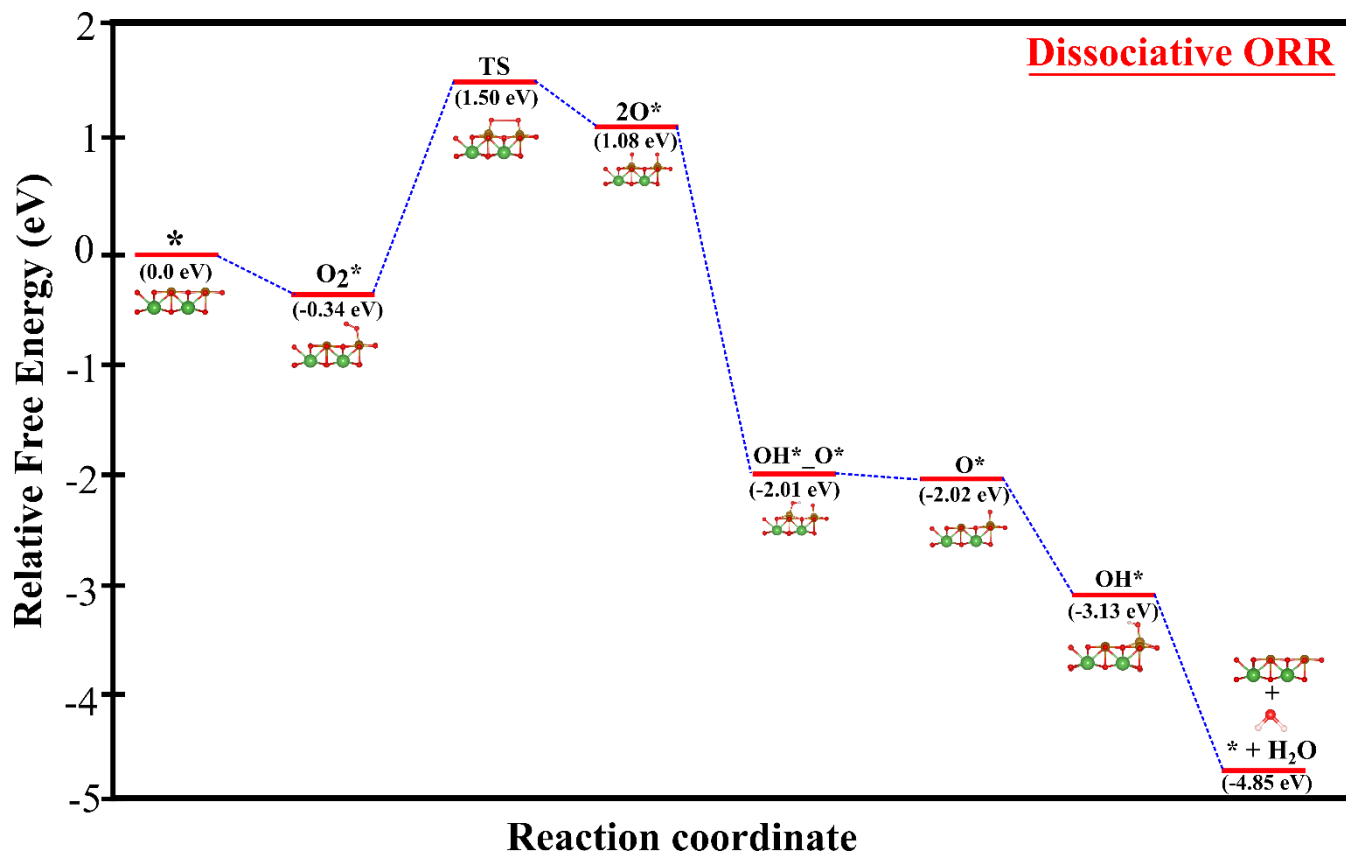


Figure 26: Potential Energy Surface (PES) of the Dissociative ORR mechanism

3.4 Theoretical Overpotential Calculation

From the minimum value of Gibbs free energy out of all the ORR steps, the overpotential for ORR can be determined for acidic media using the following equation:

$$\eta^{\text{ORR}} = \frac{\max(\Delta G \text{ of ORR steps})}{e} + 1.23$$

To achieve optimal catalytic performance, it is necessary for all the free energies of the Oxygen Reduction Reaction (ORR) steps to be equal to or greater than $4.92 \text{ eV}/4$, which corresponds to 1.23 eV . This signifies that all reaction free energies should reach zero at a balanced potential of 1.23 V . In our investigation, we observed that the first step of the adsorption of O_2 , having value of change in Gibbs free energy of -0.35 eV could potentially determine the outcome of the ORR. We computed the overpotential value using the above equation and it was calculated to be 0.88 V . This small value of overpotential depicts that 2D LaFeO_3 will be a good electrocatalyst for the reduction process of oxygen into water at the cathode of fuel cells.

3.5 Spin Density Calculations

In the present study, we conducted electron spin density calculations for all the reaction steps involved in the ORR. The variance of spin densities, which represent the difference between α and β electrons, has been depicted in Figure 27(a-f). Here, the α state is denoted as "spin up" and the β state as "spin down". Spin density calculations serve as one of the methods to anticipate the presence of unpaired electrons, or the electron cloud region, within the system under investigation. The total electron density is the summation of α and β spins of the electrons engaged in the system, and the difference between the "spin up" and "spin down" electron densities results in non-zero spin polarization and localized electron density. Electron density clouds play a significant role in electrocatalysts during the ORR by facilitating electron transfer and participating in the reaction mechanism. In the ORR, these electron density clouds aid in transferring electrons from the electrode surface to the oxygen molecules. Moreover, they create a conducive environment for the adsorption and desorption of oxygen species during the ORR. The interaction of oxygen molecules with the electrocatalyst surface involves the redistribution of electron density in both the oxygen molecule and the electrocatalyst.

In Figures 27(a-f), cyan and yellow bubbles represent electron density clouds near the Fe-atom on the surface of the 2D monolayer of the LaFeO_3 perovskite, suggesting that the Fe-site is active for the ORR. The difference in charge density quantifies the redistribution of electron charge due to the interaction between the adsorbate and the adsorbent. Yellow and cyan colours denote charge depletion and accumulation, respectively, in Figure 27. The difference in charge density indicates that the positive charge is predominantly concentrated at the center of the O atoms parallel to the O-O bond, while the negative charge is mainly concentrated on the O atoms, resulting in repulsive interactions.

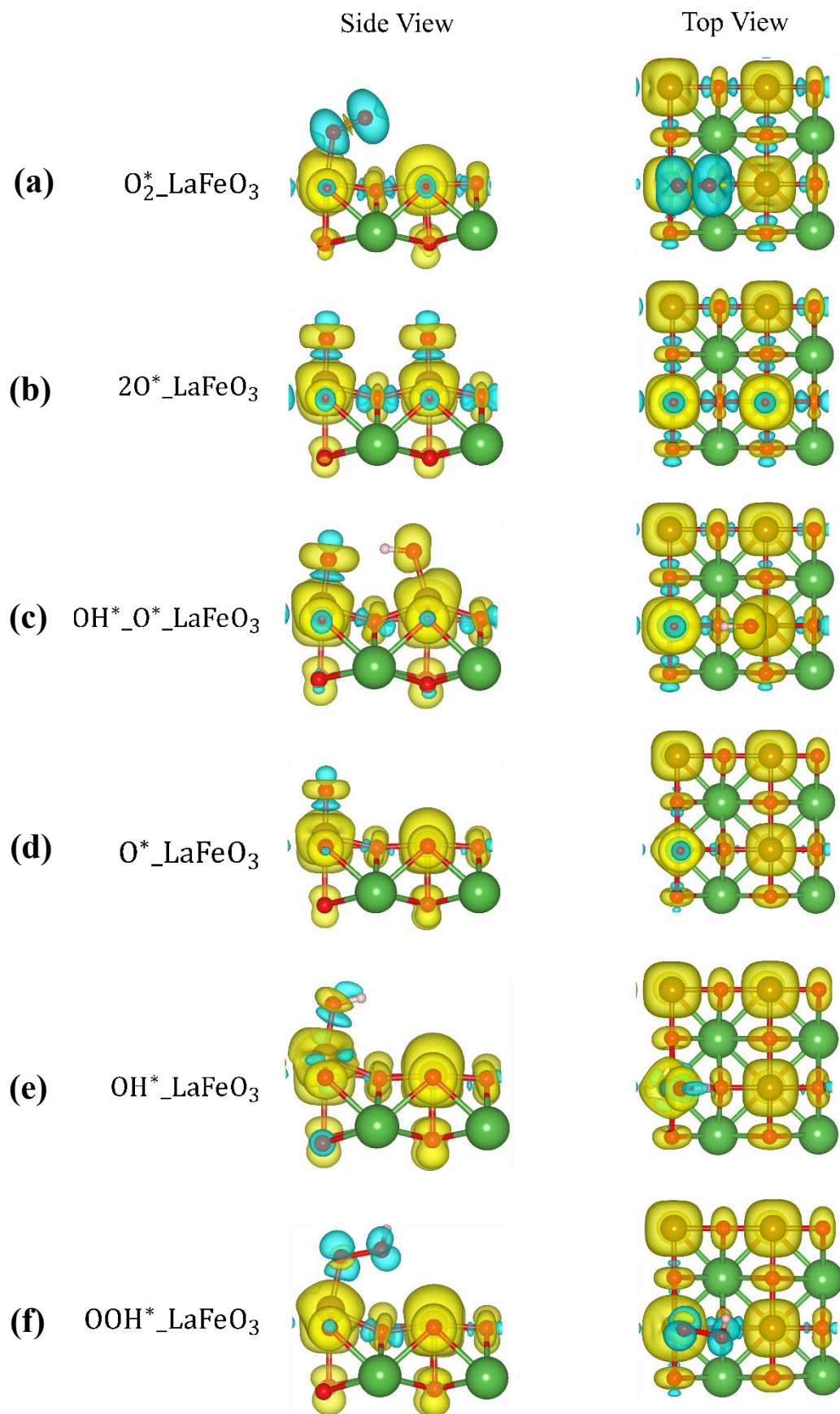


Figure 27: Electron spin density of the various equilibrium reaction intermediates during the ORR process: (a) $O_2^*_{LaFeO_3}$, (b) $2O^*_{LaFeO_3}$, (c) $OH^*_O^*_{LaFeO_3}$, (d) $O^*_{LaFeO_3}$, (e) $OH^*_{LaFeO_3}$, and (f) $OOH^*_{LaFeO_3}$.

Chapter 4

Conclusions and Scope for Future Work

4.1 Conclusions

In the present theoretical study, we conducted computational analysis on the cubic 3D LaFeO₃ perovskite material to investigate its performance towards ORR and to determine if it will be efficient in accelerating the sluggish kinetics of the reduction of oxygen at the cathode of fuel cells. At first, we computationally modelled the 3D structure of LaFeO₃ and thereafter performed structure relaxation and electronic property calculations sequentially. Electronic properties such as the electronic band structure and total density of states were computed and analysed. Our DFT study revealed the semi-metallic nature of the 3D LaFeO₃ perovskite material, with a relatively high band gap of 0.80 eV, suggesting limited potential as an electrocatalyst. This band gap was obtained through electronic band structure calculations and was later validated through the total density of states profile. Since negligible electron density was present near the Fermi energy level in the DOSs plot for 3D LaFeO₃, we concluded that charge transfer from the reactants to products will not take place readily which will in turn hamper and impede the reduction of oxygen.

To delve deeper into the catalytic activity of the LaFeO₃ perovskite material, the (001) plane was exfoliated from the 3D crystal structure of LaFeO₃ and we computationally modelled a 2D slab of the LaFeO₃ perovskite. This monolayer was then allowed to reach equilibrium and to delve deeper into the electronic properties of this 2D monolayer of the LaFeO₃ perovskite, electronic band structure and total DOS calculations were performed. A band gap of 0 eV was computed for the monolayer of LaFeO₃ which pointed towards its metallic nature. We then relied on this 2D monolayer to carry out further theoretical calculations and studied its electrocatalytic activity towards ORR. We began by computationally modelling all the reaction intermediates and then performing structure relaxation calculations on each one of these ORR intermediates.

Both the associative and dissociative mechanisms were studied and our results showed that the associative mechanism will be favourable for the reduction of oxygen on the surface of the 2D monolayer of LaFeO₃. Free energy of each reaction intermediate of ORR was calculated and it was found that all the reaction steps of the associative mechanism had negative values of free energy which reveals that all the reaction steps involved in the associative mechanism are spontaneous and thermodynamically feasible. Additionally, all the steps of the potential energy surface were downhill. These results confirm that the reduction of oxygen on the surface of 2D monolayer of the LaFeO₃ perovskite favour the associative pathway over the dissociative one. Our present calculations also reveal that the ORR on the surface of 2D monolayer LaFeO₃ has a high four-electron pathway selectivity. Furthermore, our findings, supported by CHE model-based computations, identified the 2D LaFeO₃ perovskite as a promising Pt-free ORR electrocatalyst candidate, exhibiting outstanding catalytic performance.

In summary, our research sheds light on electrocatalysis by highlighting the potential of the 2D monolayer LaFeO₃ perovskite as a promising component for fuel cells. This computationally developed material offers efficient oxygen reduction reaction kinetics, paving the way for further exploration in materials science. We anticipate that our theoretical and computational studies will inspire experimental, computational, and theoretical efforts toward the development of additional Pt-free ORR catalysts based on 2D materials.

4.2 Scope for future work

Through the research presented in this thesis, significant advancements have been made in investigating the catalytic activity of LaFeO₃ towards oxygen reduction reaction. A theoretical and computational stepping stone has been set which can be used to explore and develop other Pt-free electrocatalysts to be used in fuel cells and metal air batteries. In particular 2D perovskite materials or transition metal dichalcogenides (TMDs) can be explored for their activity towards ORR. Furthermore, the LaFeO₃ perovskite can be explored further to study how its ORR performance can be increased. This can be done in various ways such as doping either the A site or the B site in LaFeO₃, creating oxygen vacancies, strain tuning, etc. Our study revealed that the (001) plane of the LaFeO₃ perovskite is active for oxygen reduction and can be used for fuel cell applications. Further exploration, particularly through experimental techniques, would provide valuable insights. Our computational predictions align with experimental observations and this could offer a promising approach to enhance the ORR performance and conductivity of LaFeO₃. The elements that have the ability to adopt various oxidation states can substantially enhance the electronic conductivity of LaFeO₃. Another area which can be investigated pertains to the study of LaFeO₃ surfaces. An understanding of LaFeO₃'s surface chemistry can be a potential research topic. Initial efforts could involve analysing different surface sites for defects, especially oxygen vacancies, to assess if their formation energy varies depending on their location on the surface. Additionally, investigating how the formation energy of an oxygen vacancy changes from the bulk material to the surface would provide insights into their mobility through LaFeO₃. A similar examination could be conducted for potential divalent dopants (e.g., strontium, calcium, manganese, cobalt, and nickel). Calculating the solution energy of dopants in the bulk and progressively towards the surface could elucidate surface segregation phenomena observed, particularly in strontium-doped perovskites. This approach could determine if some potential dopants exhibit a tendency to segregate towards the surface of LaFeO₃. Once a comprehensive understanding of defect chemistry and dopant behaviour at the surface of LaFeO₃ is established, investigating the interaction of oxygen with various defects and dopants on the surface would provide further insights. This investigation could shed light on how LaFeO₃ catalyses the oxygen reduction reaction and its potential suitability as a base material for fuel cell applications.

REFERENCES

- (1) Owusu, P. A.; Asumadu-Sarkodie, S. A Review of Renewable Energy Sources, Sustainability Issues and Climate Change Mitigation. *Cogent Eng.* **2016**, *3*.
- (2) Pakhira, S.; Upadhyay, S. N. Efficient Electrocatalytic H₂ Evolution Mediated by 2D Janus MoSSe Transition Metal Dichalcogenide. *Sustain. Energy Fuels* **2022**, *6*, 1733–1752.
- (3) Kaygusuz, K. Energy for Sustainable Development: A Case of Developing Countries. *Renew. Sustain. Energy Rev.* **2012**, *16*, 1116–1126.
- (4) Maradin, D. Advantages and Disadvantages of Renewable Energy Sources Utilization. *Int. J. Energy Econ. Policy* **2021**, *11*, 176–183.
- (5) Chu, S.; Majumdar, A. Opportunities and Challenges for a Sustainable Energy Future. *Nature* **2012**, *488*, 294–303.
- (6) Viswanathan, B.; Scibioh, M. A. Fuel Cells: Principles and Applications. **2007**, 494.
- (7) Exner, K. S. Steering Selectivity in the Four-Electron and Two-Electron Oxygen Reduction Reactions: On the Importance of the Volcano Slope. *ACS Phys. Chem. Au* **2023**, *3*, 190–198.
- (8) Gasteiger, H. A.; Kocha, S. S.; Sompalli, B.; Wagner, F. T. Activity Benchmarks and Requirements for Pt, Pt-Alloy, and Non-Pt Oxygen Reduction Catalysts for PEMFCs. *Appl. Catal. B Environ.* **2005**, *56*, 9–35.
- (9) Nørskov, J. K.; Rossmeisl, J.; Logadottir, A.; Lindqvist, L.; Kitchin, J. R.; Bligaard, T.; Jónsson, H. Origin of the Overpotential for Oxygen Reduction at a Fuel-Cell Cathode. *J. Phys. Chem. B* **2004**, *108*, 17886–17892.
- (10) Wang, B. Recent Development of Non-Platinum Catalysts for Oxygen Reduction Reaction. *J. Power Sources* **2005**, *152*, 1–15.
- (11) Meng, H.; Zeng, D.; Xie, F. Recent Development of Pd-Based Electrocatalysts for Proton Exchange Membrane Fuel Cells. *Catalysts* **2015**, *5*, 1221–1274.
- (12) Antolini, E. Palladium in Fuel Cell Catalysis. *Energy Environ. Sci.* **2009**, *2*, 915–931.
- (13) Kulkarni, A.; Siahrostami, S.; Patel, A.; Nørskov, J. K. Understanding Catalytic Activity Trends in the Oxygen Reduction Reaction. *Chem. Rev.* **2018**, *118*, 2302–2312.
- (14) Carrette, L.; Friedrich, K. A.; Stimming, U. Fuel Cells - Fundamentals and Applications. *Fuel Cells* **2001**, *1*, 5–39.
- (15) Zhu, H.; Zhang, P.; Dai, S. Recent Advances of Lanthanum-Based Perovskite Oxides for

Catalysis. *ACS Catal.* **2015**, *5*, 6370–6385.

- (16) Ashok, A.; Kumar, A.; Bhosale, R. R.; Almomani, F.; Malik, S. S.; Suslov, S.; Tarlochan, F. Combustion Synthesis of Bifunctional LaMO₃ (M = Cr, Mn, Fe, Co, Ni) Perovskites for Oxygen Reduction and Oxygen Evolution Reaction in Alkaline Media. *J. Electroanal. Chem.* **2018**, *809*, 22–30.
- (17) Wang, Y.; Cheng, H. P. Oxygen Reduction Activity on Perovskite Oxide Surfaces: A Comparative First-Principles Study of LaMnO₃, LaFeO₃, and LaCrO₃. *J. Phys. Chem. C* **2013**, *117*, 2106–2112.
- (18) Kucharczyk, B.; Winiarski, J.; Szczygieł, I.; Adamska, K. Physicochemical Properties of LaFeO₃ Perovskite Prepared by Various Methods and Its Activity in the Oxidation of Hydrocarbons. *Ind. Eng. Chem. Res.* **2020**, *59*, 16603–16613.
- (19) Ciambelli, P.; Cimino, S.; De Rossi, S.; Lisi, L.; Minelli, G.; Porta, P.; Russo, G. AFeO₃ (A = La, Nd, Sm) and LaFe_{1-x}Mg_xO₃ Perovskites as Methane Combustion and CO Oxidation Catalysts: Structural, Redox and Catalytic Properties. *Appl. Catal. B Environ.* **2001**, *29*, 239–250.
- (20) Xiao, P.; Zhong, L.; Zhu, J.; Hong, J.; Li, J.; Li, H.; Zhu, Y. CO and Soot Oxidation over Macroporous Perovskite LaFeO₃. *Catal. Today* **2015**, *258*, 660–667.
- (21) Harker, A. H. Materials Modelling Using Density Functional Theory: Properties and Predictions, by Giustino Feliciano. *Contemp. Phys.* **2016**, *57*, 140–141.
- (22) Kresse, G.; Furthmüller, J. Efficiency of Ab-Initio Total Energy Calculations for Metals and Semiconductors Using a Plane-Wave Basis Set. *Comput. Mater. Sci.* **1996**, *6*, 15–50.
- (23) Kresse, G.; Hafner, J. Ab Initio Molecular Dynamics for Liquid Metals. *Phys. Rev. B* **1993**, *47*, 558–561.
- (24) Kresse, G.; Hafner, J. Ab Initio Molecular-Dynamics Simulation of the Liquid-Metalmorphous-Semiconductor Transition in Germanium. *Phys. Rev. B* **1994**, *49*, 14251–14269.
- (25) Joubert, D. From Ultrasoft Pseudopotentials to the Projector Augmented-Wave Method. *Phys. Rev. B - Condens. Matter Mater. Phys.* **1999**, *59* (3), 1758–1775.
- (26) John P. Perdew, Kieron Burke, Matthias Ernzerhof. Generalized Gradient Approximation Made Simple. *ACS Appl. Mater. Interfaces* **1996**, *77*, 3865–3868.
- (27) Perdew, J. P.; Chevary, J. A.; Vosko, S. H.; Jackson, K. A.; Pederson, M. R.; Singh, D. J.; Fiolhais, C. Erratum: Atoms, Molecules, Solids, and Surfaces: Applications of the Generalized Gradient Approximation for Exchange and Correlation (Physical Review B (1993) 48, 7, (4978)). *Phys. Rev. B* **1993**, *48*, 4978.

- (28) Wang, L.; Maxisch, T.; Ceder, G. Oxidation Energies of Transition Metal Oxides within the GGA+U Framework. *Phys. Rev. B - Condens. Matter Mater. Phys.* **2006**, *73*, 1–6.
- (29) Hendrik J. Monkhorst and James D. Pack. Special Points for Brillouin-Zone Integrations*. *J. Mater. Chem. APS* **1976**, *13*, 5188–5192.
- (30) Jónsson, G. H. B. P. U. H. A Climbing Image Nudged Elastic Band Method for Finding Saddle Points and Minimum Energy Paths. *J. Chem. Phys.* **2000**, *113*, 9901–9904.
- (31) Nie, Y.; Li, L.; Wei, Z. Recent Advancements in Pt and Pt-Free Catalysts for Oxygen Reduction Reaction. *Chem. Soc. Rev.* **2015**, *44*, 2168–2201.
- (32) Tripkovic, V.; Vegge, T. Potential- and Rate-Determining Step for Oxygen Reduction on Pt(111). *J. Phys. Chem. C* **2017**, *121*, 26785–26793.
- (33) Upadhyay, S. N.; Pakhira, S. Mechanism of Electrochemical Oxygen Reduction Reaction at Two-Dimensional Pt-Doped MoSe₂ material: An Efficient Electrocatalyst. *J. Mater. Chem. C* **2021**, *9*, 11331–11342.
- (34) Upadhyay, S. N.; Sardar, V. B.; Singh, A.; Kumar, V.; Pakhira, S. Elucidating the Oxygen Reduction Reaction Mechanism on the Surfaces of 2D Monolayer CsPbBr₃ Perovskite. *Phys. Chem. Chem. Phys.* **2022**, *24*, 28283–28294.
- (35) Debe, M. K. Electrocatalyst Approaches and Challenges for Automotive Fuel Cells. *Nature* **2012**, *486*, 43–51.
- (36) Beall, C. E.; Fabbri, E.; Schmidt, T. J. Perovskite Oxide Based Electrodes for the Oxygen Reduction and Evolution Reactions: The Underlying Mechanism. *ACS Catal.* **2021**, *11*, 3094–3114.
- (37) Yadav, L.; Pakhira, S. Platinum-Adsorbed Defective 2D Monolayer Boron Nitride: A Promising Electrocatalyst for O₂ Reduction Reaction. *J. Mater. Chem. C* **2023**, *11*, 15215–15232.
- (38) Singh, A.; Pakhira, S. Synergistic Niobium Doped Two-Dimensional Zirconium Diselenide: An Efficient Electrocatalyst for O₂ Reduction Reaction. *ACS Phys. Chem. Au* **2024**, *4*, 40–56.
- (39) Shein, I. R.; Shein, K. I.; Kozhevnikov, V. L.; Ivanovskiĭ, A. L. Band Structure and the Magnetic and Elastic Properties of SrFeO₃ and LaFeO₃ Perovskites. *Phys. Solid State* **2005**, *47*, 2082–2088.
- (40) Koehler, W. C.; Wollan, E. O. Neutron-Diffraction Study of the Magnetic Properties of Perovskite-like Compounds LaBO₃. *J. Phys. Chem. Solids* **1957**, *2*, 100–106.